DALROMS-NWA12 v1.0, a coupled circulation-ice-biogeochemistry modelling system for the northwest Atlantic Ocean: Development and validation

Kyoko Ohashi[1], Arnaud Laurent[1], Christoph Renkl[1], Jinyu Sheng[1], Katja Fennel[1], Eric Oliver[1]

[1]Department of Oceanography, Dalhousie University, Halifax, NS B3H 4R2 Canada

Correspondence to: Kyoko Ohashi (kyoko.ohashi@dal.ca)

2 October 2024
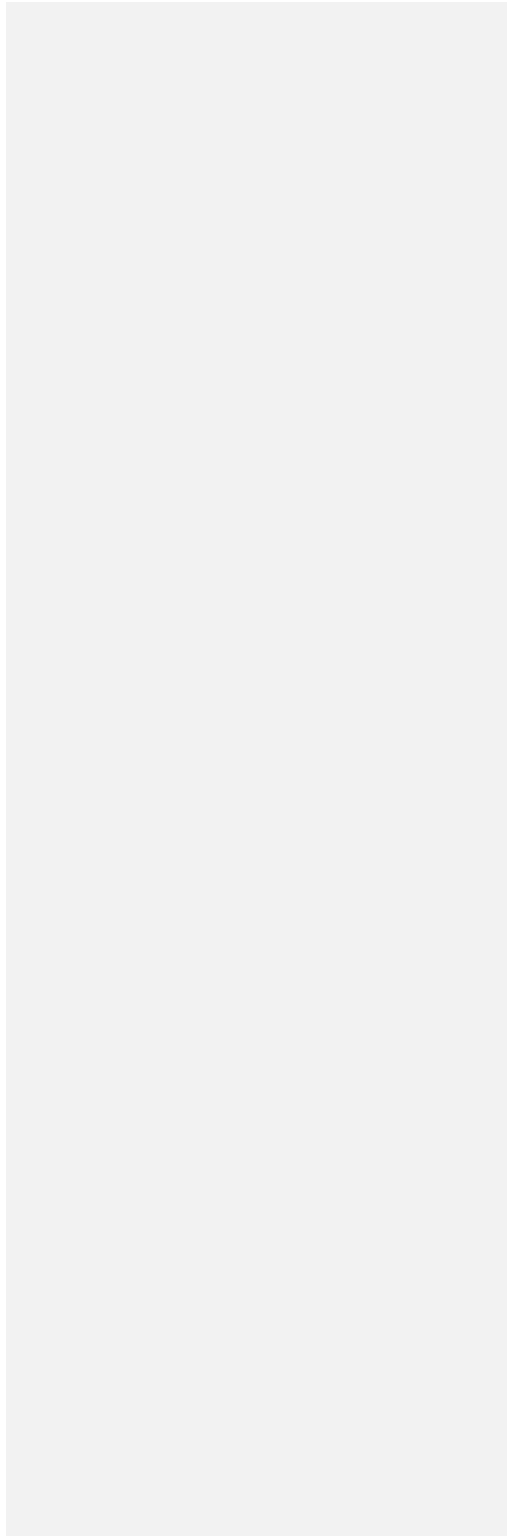
Abstract. This study presents DalROMS-NWA12 v1.0, a coupled ocean circulation-sea ice-biogeochemistry modelling system for the northwest Atlantic Ocean (NWA) in which the circulation and biogeochemistry modules are based on ROMS (Regional Ocean Modeling System). The circulation module is coupled to a sea ice module based on the Community Ice CodE (CICE), and the physical ocean state simulated by the circulation module drives the biogeochemical module. Study of the biological carbon pump in the NWA is one of the main intended applications of this model. Global atmospheric and ocean reanalyses are used respectively to force DalROMS-NWA12 at the sea surface and as part of its lateral boundary input. The modelling system is also forced by tides, riverine freshwater input, and continental runoff. The physical ocean state and sea ice from two simulations of the period 2015–2018, with and without nudging of the simulated temperature and salinity towards a blend of observations and reanalysis, are examined in this study. Statistical comparisons between model results and observations or reanalyses show the control (nudged) simulation outperforms the prognostic (un-nudged) simulation in reproducing the paths of the Gulf Stream and the West Greenland Current, as well as propagation of the estuarine plume in the Gulf of St. Lawrence. The prognostic simulation performs better in simulating the sea ice concentration. The biogeochemical module, which is run only in the control simulation, performs reasonably well in reproducing the observed spatiotemporal variations of oxygen, nitrate, alkalinity, and total inorganic carbon. To examine the effects of tides and sea ice on the physical fields in the study area, results of simulations from which either component is absent are compared to results of the prognostic simulation. In the absence of tides, Ungava Bay in summer experiences a simulated surface salinity that is higher by up to ~7 psu than in the simulation with tides, as well as changes in horizontal distributions of surface temperature and sea ice. Without coupling to the sea ice module, the circulation module produces summertime sea surface temperatures that are higher by up to ~5°C in Baffin Bay.

1 Introduction

The northwest North Atlantic Ocean (hereafter NWA) is characterized by interactions among physical and biogeochemical processes that affect the global atmosphere-ocean system. Air-to-sea flux of CO_2 per unit area is estimated to be largest in the world in the Atlantic Ocean north of 50° N, due to factors such as strong winds in winter and high primary production in spring (Takahashi et al., 2009). The sinking of particles formed during primary production has the effect of transporting atmospheric CO_2 to the deep ocean and is referred to as the biological carbon pump (BCP; Volk and Hoffert, 1985). The BCP is influenced by various physical processes over an annual cycle. The presence of sea ice in winter can, on one hand, drive upward transport of nutrients through brine rejection-induced vertical mixing (Jin et al., 2018) but on the other hand can reduce wind-induced mixing (Rainville et al., 2011) and attenuate the solar radiation (Legendre et al., 1992) by isolating the water column from the atmosphere. Seasonal changes of the mixed layer depth is another physical process that governs the BCP. Shoaling of the layer in spring, driven by freshwater input from runoff and sea ice, promotes primary production (Wu et al., 2007 and 2008; Frajka-Williams and Rhines, 2010), while deepening of the layer in winter can result in entrainment of dissolved inorganic carbon and respiratory CO_2 that had been in shallow sub-surface waters (Körtzinger et al., 2008). In the Labrador Sea, deep convection in winter is thought to be an additional pathway for removal of carbon from near-surface waters (Tian et al., 2004).

Several field programs have been conducted to quantify the major processes at work in the NWA, such as the Labrador Sea Deep Convection Experiment (The Lab Sea Group, 1998), which focused on atmospheric and physical oceanographic processes, and the Atlantic Zone Monitoring Program (Pepin et al., 2005) and its off-shelf counterpart (e.g., Yashayaev and Loder, 2017), which have made regular shipboard measurements of physical and biogeochemical (BGC) fields at fixed locations. Simultaneous measurements of physical and BGC fields at moorings (e.g., Martz et al., 2009; Strutton et al., 2011) and by profiling floats (e.g., Yang et al., 2020; Wang and Fennel 2022) have expanded the coverage of observations, which is crucial given the spatiotemporal variability in the processes that govern the BCP (Garçon et al., 2001).

66   Process-based numerical models can complement observations of oceanic processes by

67   providing four-dimensional estimates of relevant fields and by enabling experiments in which the

68   effects of key inputs are isolated or the future state of oceans under various climate scenarios are

69   simulated (Fennel et al., 2022). Early numerical studies of the NWA using coupled ocean

70   circulation-sea ice models focused mainly on specific processes, such as climatological sea ice

71   conditions (Mysak et al., 1991), sea ice variabilities on the interannual (Ikeda et al., 1996) and

72   intra-seasonal (Yao et al., 2000) time scales, and changes in sea ice and mixed layer properties

73   under different atmospheric conditions (Tang et al., 1999). As process-based numerical models

74   grew in complexity they yielded new insights, such as the role of sea ice's heat capacity in the

75   timing of ice melt (Zhang et al., 2004). Advances in computational power have led to realistic

76   simulations spanning a decade or more covering limited areas, such as the Canadian Arctic

77   Archipelago and Davis Strait (Lu et al., 2014) or the Labrador and Newfoundland Shelves (Ma et

78   al., 2016). Other ocean-ice models of areas within the NWA include that of the Gulf of St.

79   Lawrence and surrounding waters (Urrego-Blanco and Sheng, 2014; Wang et al., 2020), Hudson

80   Bay (Saucier et al., 2004), and the Labrador Sea (Pennelly and Myers, 2020). Canadian

81   government agencies have developed coupled ocean-ice or atmosphere-ocean-ice models to

82   support activities such as hazard management, with domains ranging from the regional (e.g.,

83   Smith et al., 2013 for the Gulf of St. Lawrence) to basin-wide (Dupont et al., 2015; Wang et al.,

84   2018). Other modelling studies have focused on hydrodynamics in coastal and shelf waters of the

85   NWA, such as Han et al. (1997) for the Scotian Shelf, Wu et al. (2012) for the area between the

86   Gulf of Maine and Baffin Bay, and Chen and He (2015) for the Mid-Atlantic Bight and the Gulf

87   of Maine.

88   As for coupled physical-BGC modelling studies, three-dimensional models with high resolutions

89   have generally focused on the shelf and slope areas of the NWA. Pei (2022) used a simple

90   oxygen model to study seasonal changes in dissolved oxygen over the Scotian Shelf, while more

91   complex models have been used to study the biogeochemistry and plankton dynamics of the

92   Scotian Shelf and surrounding waters (Laurent et al., 2021, Rutherford and Fennel, 2022) and the

93   Gulf of St. Lawrence (LeFouest et al., 2010; Lavoie et al., 2021). Ross et al. (2023) developed a

94   coupled physical-BGC model for the North Atlantic Ocean from the Caribbean Sea to the

95   southern Labrador Sea, designed primarily for marine resource management.

97 As coupled simulations that include more processes and cover larger extents of space and time
98 become feasible, they are expected to enhance our understanding of how the ocean functions as
99 an integrated system, as well as how this system might change under various scenarios of the
100 future climate. In this study, we present and assess a coupled ocean circulation-sea ice-BGC
101 model that has been developed recently with the primary goal of studying the interactions
102 between physical and BGC processes in the NWA, including the BCP. Advantages of this
103 model's configuration include: (a) a domain that spans the area from the Mid-Atlantic Bight to
104 Baffin Bay, allowing for a wide range of oceanographic processes that can be examined; (b) a
105 horizontal grid size of $O(1$ km) that decreases with latitude, such that the first baroclinic Rossby
106 radius of deformation (Chelton et al., 1998) is spanned by about four grid boxes everywhere; (c)
107 the use of a terrain-following vertical coordinate system, which can produce more realistic near-
108 bottom vertical mixing and bottom boundary layer structures than the step-wise bottom
109 topography of z-level grids (Ezer and Mellor, 2004); (d) the inclusion of tides (as one of the
110 model inputs) and sea ice (through coupling between the circulation and sea ice modules), both
111 of which are important elements of the ocean system in this region, and (e) the inclusion of a
112 BGC module, which enables the study of how processes such as the BCP are driven by the
113 coupled ocean circulation-sea ice system. This paper provides an assessment of the coupled
114 model's performance as well as sensitivity studies designed to elucidate the role of two physical
115 processes, tides and sea ice. The components of the coupled model and the simulations are
116 described in the next section. In Sect. 3, the results of two simulations, with and without nudging
117 of the temperature and salinity towards a blend of observations and reanalysis (referred to
118 respectively as the control and prognostic simulations), are described and quantitatively
119 compared to observations or reanalysis. In addition, depth vs. time plots of simulated
120 temperature are used to qualitatively assess the model's performance in reproducing the effects
121 of winter convection in the Labrador Sea. In Sect. 4, the roles of tides and sea ice in the physical
122 fields of the NWA are examined by comparing the results of two additional simulations, one
123 without tidal forcing and the other without the simulation of sea ice, to results of the prognostic
124 simulation described in Sect. 3. A summary of our findings is presented in the concluding
125 section.

2 Model setup and forcing

The coupled circulation-sea ice-BGC modelling system used in this study consists of three modules: an ocean circulation module based on ROMS (Regional Ocean Modeling System, version 3.9; Haidvogel et al., 2008), a sea ice module based on CICE (Community Ice CodE, version 5.1; Hunke et al., 2015), and a BGC module within ROMS based on the work of Fennel et al. (2006, 2008) with updates as described by Laurent et al. (2021). The circulation and sea ice modules are coupled using the software MCT (Model Coupling Toolkit, version 2.10; Jacob et al., 2005; Larson et al., 2005) in a manner similar to Kristensen et al. (2017). Yang et al. (2023) found good agreement between simulated and observed values of tides and storm surges simulated by a barotropic version of the ocean circulation module.

ROMS is a three-dimensional (3D) numerical circulation model with a free surface and the terrain-following S-coordinate system (originally developed by Song and Haidvogel (1994)) in the vertical. The vertical layers are placed more densely near the surface and bottom in deep waters, and more uniformly in shallow waters. In this study ROMS has 40 vertical S-layers, whose configuration is described in Appendix A. ROMS and CICE use the same horizontal grid and bathymetry, with the domain covering the area between ~81° W and ~39° W and between ~33.5° N and ~76° N (Fig. 1a). The grid resolution in the east-west direction is 1/12°, resulting in grid box dimensions of ~8 km on each side near the grid's southern boundary and ~2 km on each side near the northern boundary.

The model bathymetry is derived from the 1/240°-resolution data set GEBCO_2019 (GEBCO Compilation Group, 2019). After the GEBCO data were linearly interpolated onto the model grid, the Shapiro filter (Shapiro, 1975) was applied to seamounts in deep waters from ~67.5° W to ~42° W and from ~34° N to ~48° N to reduce currents caused by spurious pressure gradients. No other smoothing was applied to the bathymetry. To avoid model instability caused by strong currents entering the model domain at an angle, the model bathymetry and land-sea mask in the first four grid boxes from each lateral boundary were set to the same values as in the fifth grid box from the boundary.

The advection schemes used in ROMS for physical fields are: (a) the third-order upstream scheme for horizontal advection of physical tracers and 3D momentum and (b) the fourth-order

155 centered scheme for horizontal advection of two-dimensional momentum and for vertical

156 advection of physical tracers and 3D momentum. The horizontal eddy viscosity and diffusivity in

157 ROMS are set to zero because the third-order upstream scheme generates some numerical

158 diffusion which is large enough to eliminate small-scale features associated with numerical

159 noise. Vertical mixing is parameterized using the "2.5-level" scheme of Mellor and Yamada

160 (1982) with modifications as described by Allen et al. (1995). The time step is 6 seconds for the

161 external (barotropic) mode and 120 seconds for the internal (baroclinic) mode.
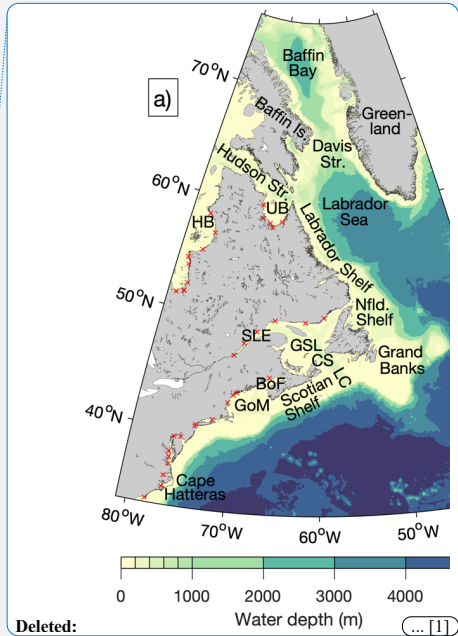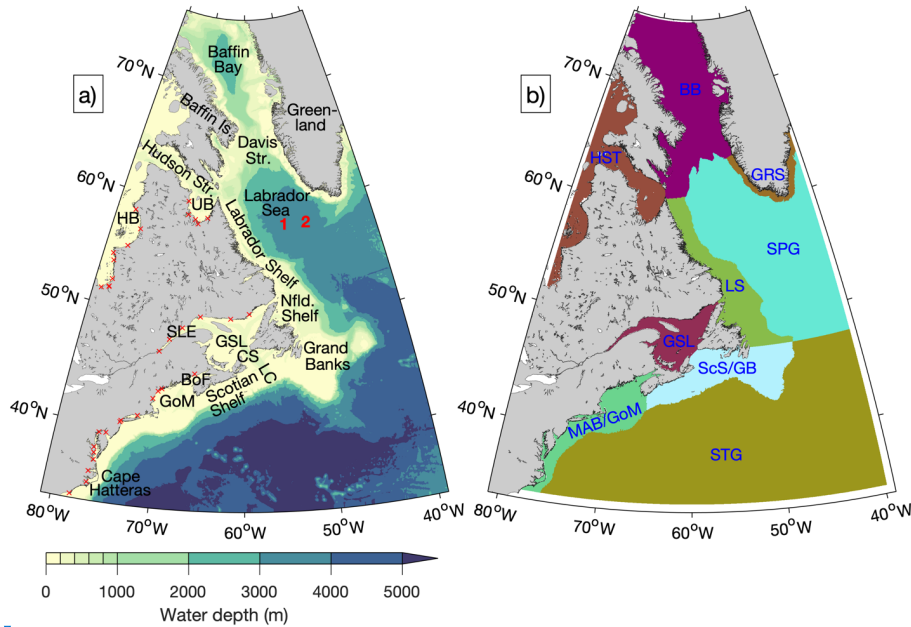
162

163 **Figure 1. (a)** Model domain and bathymetry. Locations of river mouths are indicated by red X marks. Locations for

164 which depth profiles of simulated temperature are shown in Fig. 16 are indicated by numbers in red. Abbreviations

165 are used for: Island (Is.), Strait (Str.), Hudson Bay (HB), Ungava Bay (UB), Newfoundland (Nfd.), St. Lawrence

166 Estuary (SLE), Gulf of St. Lawrence (GSL), Cabot Strait (CS), Laurentian Channel (LC), Bay of Fundy (BoF), and

167 Gulf of Maine (GoM). **(b)** Regions in which metrics of model performance are calculated. The regions are: GRS

168 (Greenland Shelf), HST (Hudson Strait), BB (Baffin Bay), LS (Labrador Shelf), SPG (Subpolar Gyre), GSL (Gulf of

169 St. Lawrence), ScS/GB (Scotian Shelf/Grand Banks), MAB/GoM (Mid-Atlantic Bight/Gulf of Maine), and STG

170 (Subtropical Gyre). Areas within 10 grid points of lateral boundaries are excluded from the error metric calculations.

Atmospheric fields used to drive the coupled model are derived from the hourly reanalysis data set known as ECMWF Reanalysis v5 (ERA5; Hersbach et al., 2018) which has a horizontal grid spacing of 1/4º. Within ROMS, the bulk flux scheme of Fairall et al. (1996a, 1996b) is used to calculate the surface fluxes of heat and fresh water. Lateral open boundary conditions are specified using the explicit scheme of Chapman (1985) for sea surface elevation, the Shchepetkin scheme (Mason et al., 2010) for the normal component and the implicit scheme of Chapman (1985) for the tangential component of depth-averaged currents, and the adaptive scheme of Marchesiello et al. (2001) for the normal and tangential components of depth-varying currents as well as all tracers. In the adaptive boundary condition, the nudging time scale is three days for inflow and 360 days for outflow. The values of currents, temperature, salinity, and sea surface elevation specified at the lateral boundaries are derived from the daily fields of Copernicus global 1/12° oceanic and sea ice reanalysis (GLORYS12V1, hereafter GLORYS; Lellouche et al., 2021) for the simulation period. In order to ensure that the simulated ocean states near lateral open boundaries are as realistic as possible, the lateral boundary conditions of currents, temperature, and salinity are supplemented by nudging the simulated values near boundaries towards GLORYS values. The nudging time scale is three days at the grid point closest to a lateral boundary and decreases linearly to zero over ten grid points moving away from the boundary. Tidal elevation and currents are specified at the lateral boundaries from the global tidal model solution TPXO9v2a (an updated version of the model by Egbert and Erofeeva (2002)), with a horizontal grid size of 1/6º and 15 tidal constituents.

Riverine freshwater input from 35 rivers (Table 1) is specified as volume flux through the bottom of a model grid cell (www.myroms.org/forum/viewtopic.php?t=5156). Each river is represented by a channel normal to the model's coastline, at the head of which the surface elevation, vertical velocity, and tracer values are adjusted according to the river discharge. The river water has a salinity of 0.4 psu (salinity in the Practical Salinity Scale is dimensionless but we use the unit "psu" for clarity) and a temperature equal to that of the GLORYS sea surface temperature at the grid point closest to the river mouth. For the St. Lawrence River, we use the monthly-mean discharge at Quebec City estimated by the St. Lawrence Global Observatory (2023) using the regression model of Bourgault and Koutitonsky (1999). For all other rivers, we use the monthly-mean data set of Dai (2017) that was updated in May 2019, substituting climatological values

217 calculated over the period 1900–2018 for months with no data. Freshwater flux across coastlines
218 due to the melting of ice and snow over land is specified as an addition to the sea surface height
219 and the surface freshwater flux at the appropriate model grid boxes. This freshwater flux is
220 derived from the monthly data set of Bamber et al. (2018), who combined satellite observations
221 of glaciers with the output of a regional climate model. A monthly climatology of this data set,
222 which covers the period 1958–2016, is used in simulations of the period after December 2016.
223 Both the riverine and continental freshwater fluxes are converted to "pseudo-means" (monthly

224 **Table 1.** Names and discharge locations of rivers in the coupled model.

River	Lon. (° W)	Lat. (° N)	River	Lon. (° W)	Lat. (° N)
Innuksuac	78.06	58.42	Saguenay	69.72	48.06
Nastapoca	76.56	56.91	St. Lawrence	70.81	46.94
Great Whale	77.81	55.28	Saint John	66.14	45.32
Roggan	79.56	54.37	Androscoggin	69.89	43.78
La Grande + Sakami	79.22	53.78	Saco	70.31	43.54
Eastmain	78.72	52.23	Merrimack + Pemigewasset	70.81	42.87
Rupert	78.89	51.56			
Nottaway	78.89	51.51	Connnecticut	72.31	41.26
Harricana	79.89	51.30	Hudson	74.06	40.63
Arnaud	69.64	60.04	Passaic (Ramapo)	74.14	40.50
Leaf	69.39	58.90	Delaware + Beaver Kill	75.47	39.42
Koksoak (Caniapiscau + Mélèzes)	68.14	58.55	Susquehanna	76.22	39.35
			Potomac	76.47	38.05
False + Whale	67.64	58.20	Rapidan + Rappahannock	76.39	37.59
George	66.14	58.77			
Petit Mécatina	59.39	50.62	James	76.31	36.99
Natashquan	61.89	50.19	Roanoke	76.64	35.99
Moisie	65.97	50.24	Neuse (Contentnea)	76.64	35.04
Manicouagan + Outardes	68.22	49.17	Cape Fear	78.14	33.87

225 means that are adjusted such that daily-mean values temporally interpolated from them, when

226 summed over a month, results in the true monthly means) following Killworth (1996). Another

227 source of salt/freshwater flux at the sea surface is sea ice, which is a source of salt through brine

228 rejection at the time of freezing and a source of fresh water at the time of melting. Lateral

229 movement of sea ice results in these two surface fluxes occurring at different locations.

230 The sea ice model CICE consists of four main components: (a) a thermodynamic component that

231 calculates local growth or decay of sea ice due to snowfall and heat fluxes (Bitz and Lipscomb,

232 1999; Briegleb and Light, 2007); (b) a dynamic component that calculates the material properties

233 of the ice (Hunke and Dukowicz, 1997; Bouillon et al., 2013); (c) a transport component that

234 calculates the horizontal advection of the ice (Lipscomb and Hunke, 2004); and (d) a component

235 that calculates the distribution of ice among thickness categories due to ridging and mechanical

236 processes (Hunke et al., 2015). There are seven ice layers and five ice thickness categories. We

237 implemented the clamped boundary condition, in which GLORYS-derived values of sea ice

238 concentration (as a fraction of the model grid box area) and thickness are specified at the model's

239 lateral open boundaries. The sea ice specified at the lateral boundaries is uniformly covered with

240 snow of 0.2-m thickness. The time step in CICE is 1200 seconds.

241 Coupling between ROMS and CICE via MCT occurs every 1200 seconds, equivalent to every 10

242 internal time steps in ROMS and every time step in CICE. At each coupling step, ROMS sends

243 CICE the ERA5-derived atmospheric fields that drive both modules, as well as ROMS-simulated

244 values of currents, sea surface tilt, and sea-surface values of temperature and salinity. CICE

245 sends ROMS the ice-attenuated value of shortwave radiation and ice-ocean fluxes of stress, heat,

246 and salt or freshwater.

247 The BGC module includes the nitrogen cycle (Fennel et al., 2006), the carbonate system (Fennel

248 et al., 2008), and oxygen (Fennel et al., 2013). Particulate organic matter variables

249 (phytoplankton, zooplankton, and detritus) are split into small and large size classes, and rates of

250 biological processes are temperature-dependent (Laurent et al., 2021). The HSIMT advection

251 scheme (Wu and Zhu, 2010), which ensures no spurious negative values occur, is used for both

252 horizontal and vertical advection of BGC tracers. Initial and boundary conditions for nitrate,

253 phosphate, dissolved inorganic carbon, alkalinity, and oxygen are interpolated from the

254 climatology of GLODAP (Global Ocean Data Analysis Project; Lauvset et al., 2021) and set to a
255 small constant value for all other biogeochemical variables.

256 Four simulations will be examined in this paper. In the control simulation (hereafter Ctrl), the
257 ocean temperature and salinity at all grid points are nudged with a restoring time scale of 60 days
258 toward the monthly data set of in situ observations known as CORA (COriolis dataset for Re-
259 Analysis; Cabanes et al., 2013) above the 2000-m depth and GLORYS below 2000 m (where
260 CORA data are not available). The control simulation includes biogeochemistry. The second
261 simulation is a prognostic one (hereafter Prog), i.e., without any nudging of the simulation. There
262 are three reasons for presenting these simulations: 1) the ways in which either simulation
263 outperforms the other can shed light on potential ways in which the model can be improved; 2)
264 Ctrl, by including nudging of the temperature and salinity, produces a physical state of the ocean
265 that is generally realistic and acts as a foundation for the biogeochemical simulation; and 3) this
266 modelling system is being used in regional climate simulations (Renkl et al., in prep.), and the
267 lack of an option to nudge simulations of future conditions necessitates assessment of a
268 prognostic simulation. The performances of Ctrl and Prog will be evaluated in the next section.
269 Two more simulations are carried out for the sensitivity studies discussed in Sect. 4. Both are
270 identical to Prog but one is made without the specification of tidal elevation and currents at the
271 lateral boundaries (hereafter NoTides) and the other is made without coupling of ROMS to CICE
272 (hereafter NoIce). Configurations of the simulations are summarized in Table 2. All simulations
273 are made from 1 September 2013 to 31 December 2018 and are initialized with an ice-free ocean
274 in which the ocean's state consists of GLORYS fields for 1 September 2013 interpolated to the
275 model grid. The simulation results of January 2015 onwards (December 2014 onwards in the
276 case of seasonal averages) will be discussed in the following sections.

277   **Table 2**. Descriptions of the simulations discussed in this study.

Simulation name	Description	Temperature & salinity nudging	Tidal forcing at lateral boundaries	Coupling to sea ice model
Ctrl	Control	On	On	On
Prog	Prognostic	**Off**	On	On
NoTides	No tidal forcing	**Off**	**Off**	On
NoIce	No sea ice simulation	**Off**	On	**Off**

278   **3 Model results and evaluation**

279   **3.1 Simulated currents, temperature, and salinity**

280   We first examine four-year (1 January 2015–31 December 2018) averages of currents, salinity,

281   and temperature produced by DalROMS-NWA12 v1.0 in runs Ctrl and Prog (Figs. 2 and 3

282   respectively). Both model runs reproduce the major features of the circulation in this region.

283   They include: (a) the East and West Greenland Currents forming a clockwise flow around the

284   southern tip of Greenland; (b) bifurcation of the West Greenland Current, with one branch

285   continuing northward along the west coast of Greenland and the other flowing westward across

286   the Labrador Sea; and (c) the westward flow across the Labrador Sea merging with the

287   southward Baffin Island Current out of Baffin Bay and southeastward flow out of Hudson Strait

288   to form the Labrador Current, the equatorward limb of the North Atlantic Subpolar Gyre. This

289   current has branches along the Labrador coast and the shelf break. Near the Grand Banks, the

290   Labrador Current meets the poleward Gulf Stream, the poleward limb of the North Atlantic

291   Subtropical Gyre. Both simulations also reproduce the relatively cold and fresh water over

292   continental shelves, with especially low values of salinity in Hudson Bay and the St. Lawrence

293   Estuary. The three major differences between the simulations are that: (a) the bifurcation of the

294   West Greenland Current has a stronger northward branch in Prog; (b) the Gulf Stream in Prog is

295   closer to the continental shelf; and (c) the Gulf of St. Lawrence is warmer and saltier in Prog,

296   both at the surface and in model results interpolated to the 100-m depth. As discussed below,

297   comparison of model results to observations or reanalysis suggests the results of Ctrl are more

298   realistic than those from Prog. Seasonal-means of these simulated fields, shown in Appendix B,

299   indicate that differences between the simulations are more prominent in summer than in winter.

3.2 Model performance for currents, temperature, and salinity

To assess the model's performance in simulating currents, temperature, and salinity, we divide the model domain into nine regions (Fig. 1b) and calculate metrics in each region for model results at the sea surface and interpolated to the 100-m depth. Within a given region, each model grid point is weighted by its horizontal area when regional averages are calculated. The areas along the model's lateral boundaries in which the simulated tracers and currents are nudged towards GLORYS are not included in the calculations.

To quantify model performance for temperature and salinity at the sea surface, root-mean-square errors (RMSE) of monthly-mean model results are calculated with respect to monthly means of observations that are linearly interpolated to the model grid. Temperature and salinity at the surface are compared to 1/4º-grid analysed data sets that combine satellite and in situ observations: the daily data set OISST (Optimum Interpolation Sea Surface Temperature, v2.0 for 2015–2017 and v2.1 for 2018; Huang et al., 2021) for temperature and the weekly data set SMOS (Soil Moisture Ocean Salinity; Buongiorno Nardelli et al., 2016) for salinity. For model results interpolated to the 100-m depth, where gridded observational data sets are not available, root-mean-square differences (RMSD) of temperature and salinity are calculated with respect to their respective GLORYS values. It should be noted that GLORYS is based on simulations that do not include tides (Lellouche et al., 2018), which may affect the accuracy of its temperature and salinity distributions in addition to that of its currents, particularly over areas with strong tidal currents. It should also be noted that the oceanographic observations used in generating GLORYS are highly sparse in both time and space. As a result, data assimilation cannot eliminate biases associated with the exclusion of tidal forcing in the monthly mean fields of GLORYS.

The RMSE and RMSD of temperature from the two simulations (Figs. 4–5) are similar over the northern part of the model domain in that the largest errors tend to occur at the surface in GRS (Greenland Shelf) throughout the year, and in HST (Hudson Strait) and BB (Baffin Bay) during the summer. Within these three areas, the largest values of RMSE/RMSD occur in HST at the surface (about 3.5ºC in Ctrl and 2.9ºC in Prog, both in July). The corresponding biases of surface temperatures (not shown) indicate a tendency for overestimation (+0.3ºC–+2.2ºC in GRS, and -0.4ºC–+1.9ºC and -0.5ºC–+1.0ºC during summer in HST and BB respectively for Prog). Thus,
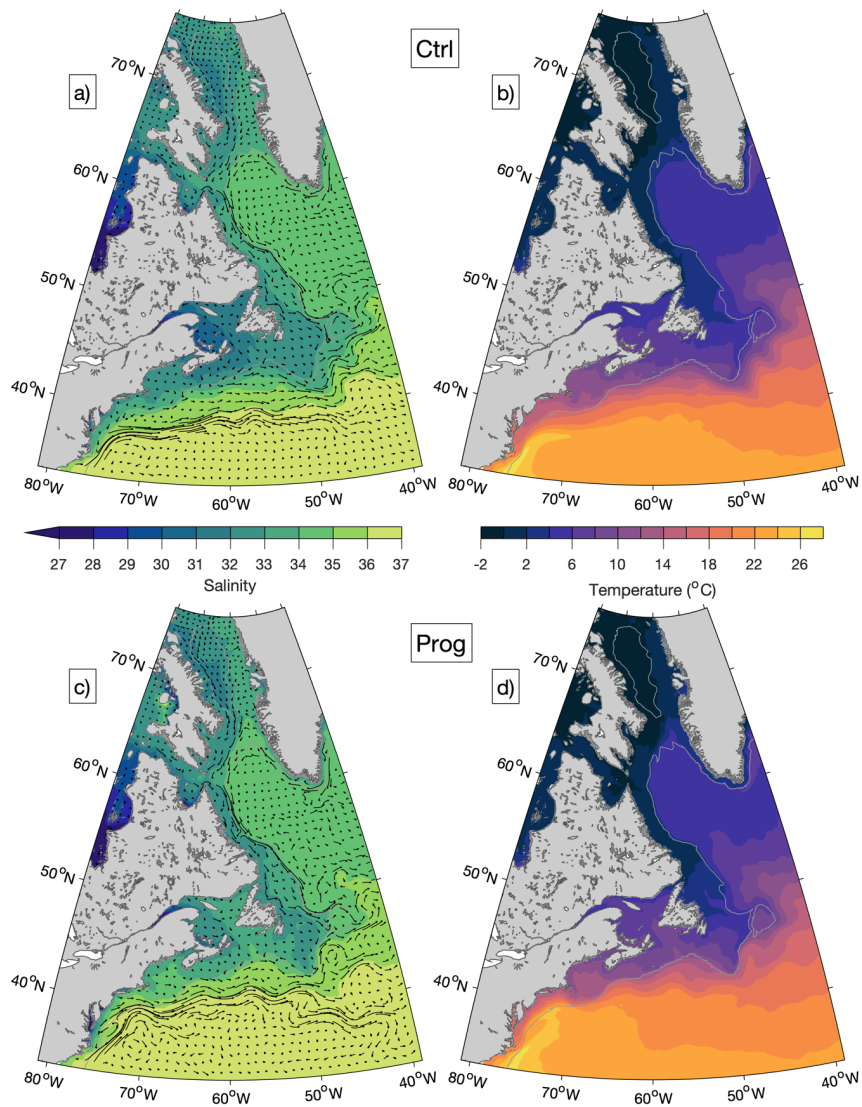
333
334
335   **Figure 2.** Temporal-mean salinity **(a, c)** and temperature **(b, d)** at the sea surface, averaged over 2015–2018, from
336   runs Ctrl **(a, b)** and Prog **(c, d)**. Also shown in panels **(a)** and **(c)** are trajectories representing displacement over five
337   days due to currents at the sea surface averaged over 2015–2018, shown at every 24 model grid points. The gray
338   contour line represents the 1000-m water depth.
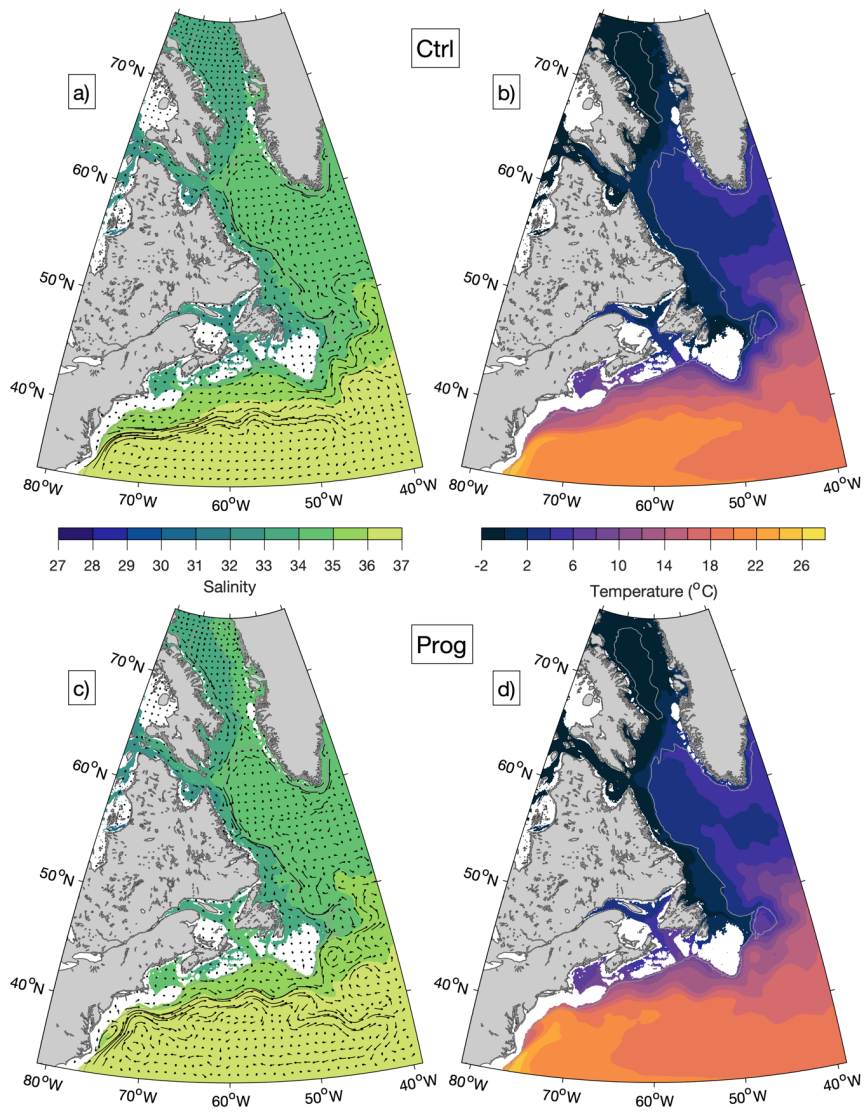
339
340
341   **Figure 3.** Similar to Fig. 2 but for model results interpolated to the 100-m depth.
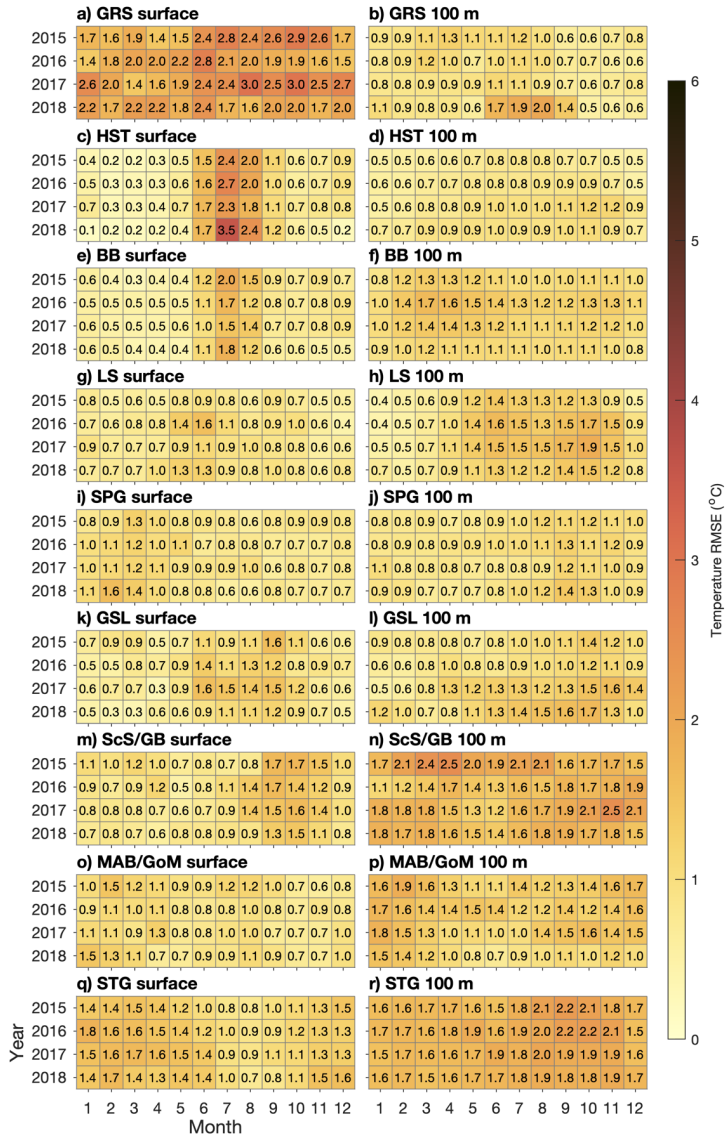
342
343
344 **Figure 4.** Root-mean-square-errors/differences of temperatures (°C) simulated in Ctrl, calculated for the regions

345 shown in Fig. 1b with respect to the observation-derived OISST data set at the surface and GLORYS reanalysis for

346 model results interpolated to the 100-m depth.
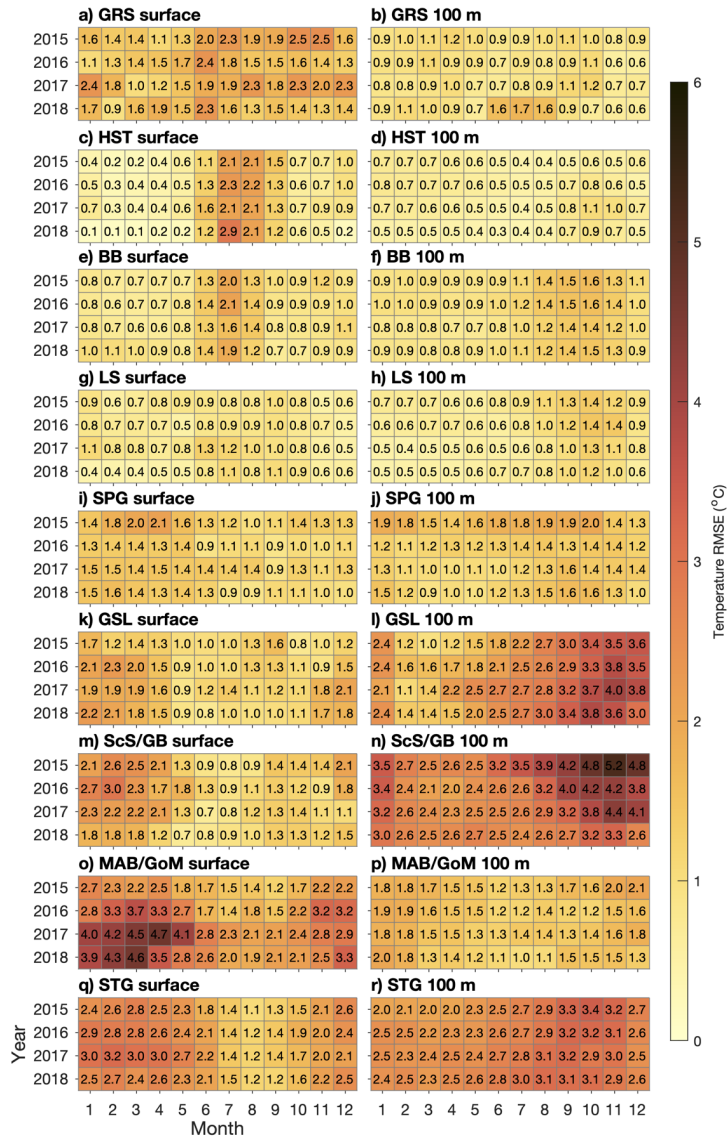
347
348
349 **Figure 5.** Similar to Fig. 4 but for temperatures simulated in Prog.
350

351   the largest errors occur near the model's lateral open boundaries, during periods when sea ice

352   (which would tend to keep the temperature near freezing) is less in HST and BB, and at the

353   surface where the performance metrics are calculated with respect to an independent

354   observational data set instead of GLORYS which is also used as lateral boundary input. This

355   suggests GLORYS as a possible source of model errors, although a detailed examination is

356   beyond the scope of this study. The slightly larger RMSE of the simulated surface temperature in

357   Ctrl than in Prog over these areas may be related to the larger underestimation of sea ice in Ctrl,

358   which will be discussed in Sect. 3.3.

359   Further south, in SPG (Subpolar Gyre), the RMSE/RMSD are smaller in Ctrl than in Prog. The

360   RMSE at the surface has the range of 0.6–1.6°C in Ctrl and 0.9–2.1°C in Prog, and the RMSD for

361   model results interpolated to the 100-m depth has the range of 0.7–1.4°C in Ctrl and 0.9–2.0°C in

362   Prog. This suggests the West Greenland Current simulated in Ctrl, in which the branch of the

363   current that separates from the Greenland coast dominates, and its associated temperature

364   distribution are more realistic. The RMSE/RMSD in LS (Labrador Shelf) are similar between the

365   simulations, ranging from 0.4 to 1.9°C in Ctrl and from 0.4 to 1.4°C in Prog.

366   The results of Ctrl clearly outperform those of Prog over the southern part of the model domain,

367   with a maximum RMSE/RMSD of ~2.5°C in the former and ~5.2°C in the latter, both occurring

368   in ScS/GB (Scotian Shelf/Grand Banks) for model results interpolated to the 100-m depth. This

369   indicates the Gulf Stream simulated in Ctrl, flowing further from the coast than in Prog (Figs. 2–

370   3), is more realistic. In addition to STG (Subtropical Gyre) where the Gulf Stream itself flows,

371   the RMSE/RMSD in Ctrl are smaller both at the surface and the 100-m depth in ScS/GB,

372   MAB/GoM (Mid-Atlantic Bight/Gulf of Maine), and GSL (Gulf of St. Lawrence), all of which

373   are influenced by the warm and salty slope water of which the Gulf Stream water is one

374   component (Gatien, 1976). The influence of the slope water extending into the GSL at the 100-m

375   depth (which can also be seen in Fig. 3) is consistent with the observed (e.g., Richaud et al.,

376   2016) intrusion of slope water into the Gulf of St. Lawrence along the Laurentian Channel.

377   The RMSE and RMSD of salinity for both simulations (Figs. 6–7) in the northern part of the

378   domain are similar to those of temperature in that they tend to be largest at the surface in

379   summer, especially in HST where the RMSE has maximum values of ~2.7 psu in Ctrl and ~3.7
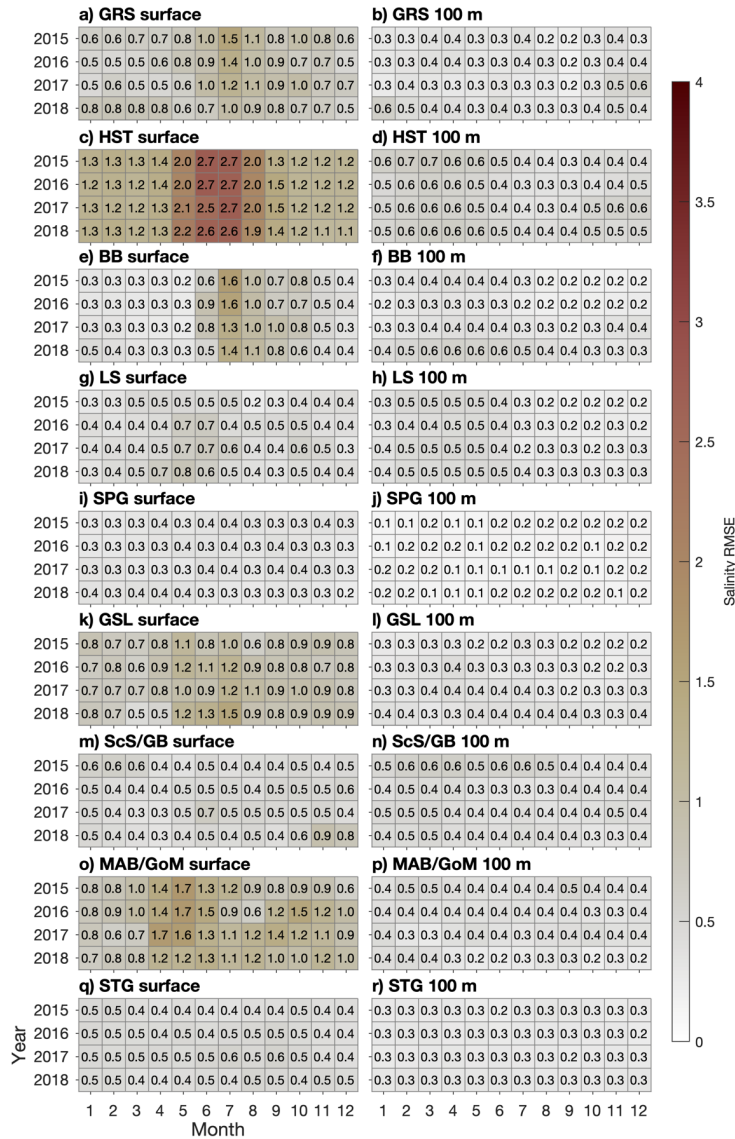
380
381
382 **Figure 6.** Root-mean-square-errors/differences of salinity (psu) simulated in Ctrl, calculated for the regions shown

383 in Fig. 1b with respect to the observation-derived SMOS data set at the surface and GLORYS reanalysis for model

384 results interpolated to the 100-m depth.
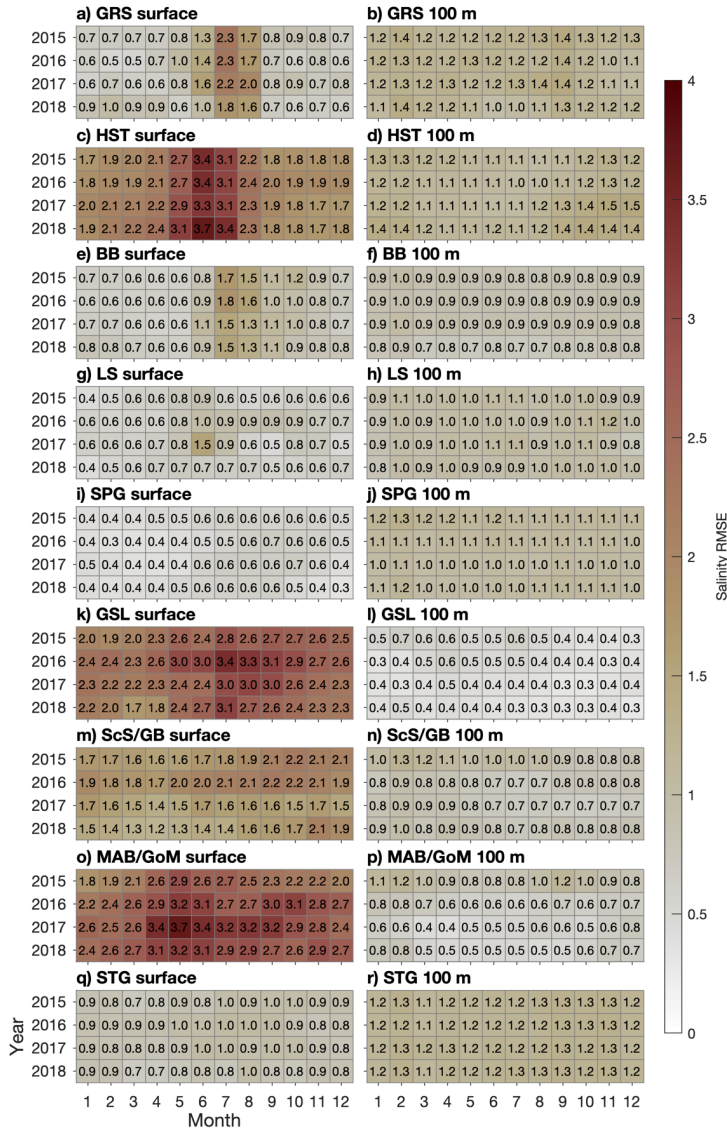
385
386
387 **Figure 7.** Similar to Figure 6 but for salinity simulated in Prog.
388

389 psu in Prog. In contrast to the temperature metrics, the surface salinity metrics in GRS undergo

390 an annual cycle similar to those in HST and BB, being larger during summer and fall than during

391 the rest of the year. During the months when the RMSE are largest, the surface salinity biases for

392 Prog are negative in GRS and BB (~-1.0 psu) and positive in HST (up to ~+1.5 psu). In SPG and

393 LS the RMSE/RMSD are generally smaller in Ctrl than in Prog (0.1–0.8 psu for Ctrl and 0.4–1.5

394 psu in Prog for the two regions combined), which is consistent with the metrics for temperatures

395 discussed above.

396 In the southern part of the domain, Ctrl has much smaller RMSE than Prog in GSL, ScS/GB, and

397 MAB/GoM (e.g., the maximum value is ~1.7 psu for Ctrl and ~3.7 psu for Prog in MAB/GoM).

398 The corresponding biases for Prog in these areas are consistently positive (up to ~+3.3 psu in

399 GSL), indicating overestimation. However, within GSL, the 2015–2018 mean of summer surface

400 salinity simulated by Prog is lower than its counterpart from Ctrl by up to ~3.5 psu in the St.

401 Lawrence Estuary, but higher by ~2.0 psu further downstream in the Gulf of St. Lawrence (not

402 shown). This suggests the model is not able to fully reproduce the propagation of low-salinity

403 water from the St. Lawrence Estuary (where the salinity is underestimated) to areas downstream

404 of it (where the salinity is overestimated).

405 A possible cause of this discrepancy between observed and simulated salinity values in the St.

406 Lawrence Estuary-Gulf system is spurious diapycnal mixing generated by the third-order

407 upstream advection scheme used for tracers in this study (Marchesiello et al., 2009). We found

408 that switching to the fourth-order Akima scheme (with a horizontal eddy diffusivity of 5 m^2 s^{-1})

409 leads to more realistic simulations of three-dimensional salinity distributions and sea ice

410 distributions in the Gulf, but this option was not pursued further because the scheme is prone to

411 over- or under-shooting, which resulted in patches of unrealistic tracer values in areas such as the

412 Grand Banks where strong horizontal gradients occur. The same problem was reported by

413 Naughten et al. (2017) in simulating circulation in the Southern Ocean using ROMS and CICE.

414 A potential solution is a fourth-order advection scheme with a flux limiter to eliminate the

415 spurious over- and under-shooting, as demonstrated by Sheng (2002) for a z-level ocean model.

416 For currents, the model performance is evaluated using a metric known as ε^2 (Schwab et al.,

417 1989; Urrego-Blanco and Sheng, 2014):

429
$$\varepsilon^2 = \frac{\sum_{i=1}^{N}\left[\left(U_i^O - \overline{U_i^O} - U_i^M + \overline{U_i^M}\right)^2 + \left(V_i^O - \overline{V_i^O} - V_i^M + \overline{V_i^M}\right)^2\right]}{\sum_{i=1}^{N}\left[\left(U_i^O - \overline{U_i^O}\right)^2 + \left(V_i^O - \overline{V_i^O}\right)^2\right]},$$ (1)

430   where the superscripts O and M denote observed and simulated values respectively, overbars

431   denote spatial averaging over each validation region, and the summation is made over the

432   validation region. Thus, this metric combines errors for the zonal and meridional current

433   components and assesses model performance in terms of spatial averages as well as at individual

434   points, with a value of zero corresponding to perfect agreement between model results and

435   observations. The metric is calculated with respect to GLORYS both at the surface and for model

436   results interpolated to the 100-m depth.

437   For both simulations, values of ε^2 (Figs. 8–9) in the southern part of the model domain are

438   generally smaller in Ctrl than in Prog (e.g., about 0.7–1.3 for Ctrl vs. 1.0–2.2 for Prog in STG),

439   consistent with the more realistic simulation of the Gulf Stream due to the nudging of salinity

440   and temperature in Ctrl. In SPG and LS, values of ε^2 are similar between the regions and smaller

441   in Ctrl than in Prog (about 0.4–1.1 in Ctrl and 0.5–1.6 in Prog for the two regions combined).

442   This suggests the Labrador Current is more realistic in Ctrl than in Prog, which is consistent with

443   the conclusion drawn from the temperature metrics that the separation of the West Greenland

444   Current from the Greenland coast is simulated more accurately in Ctrl.

445   The model errors for both runs are largest in HST, mostly due to the southeastward flow along

446   the south side of Hudson Strait being stronger in the model than in GLORYS (not shown).

447   Taking as an example the 2015–2018 mean of monthly-mean currents produced by Prog in

448   September, the southeastward flow is stronger than that in GLORYS by ~0.25 m s^{-1} at the surface

449   and ~0.15 m s^{-1} at the 100-m depth. One possible reason for this large discrepancy is that the

450   model is likely to be unable to accurately simulate the circulation in Hudson Bay, which is the

451   source of the southeastward flow through Hudson Strait. Circulation in the Bay consists of

452   several gyres and is sensitive to river discharge (Ridenour et al., 2019). Our model domain

453   includes only the eastern part of the Bay (Fig. 1a) and, due to a lack of observations, we use

454   climatological discharge (mostly calculated from observations in the 1960s or 1970s) for all but

455   one of the ten rivers emptying into the eastern Bay; these factors cast doubt on the model's

456   ability to realistically simulate the flow within and out of the Bay.
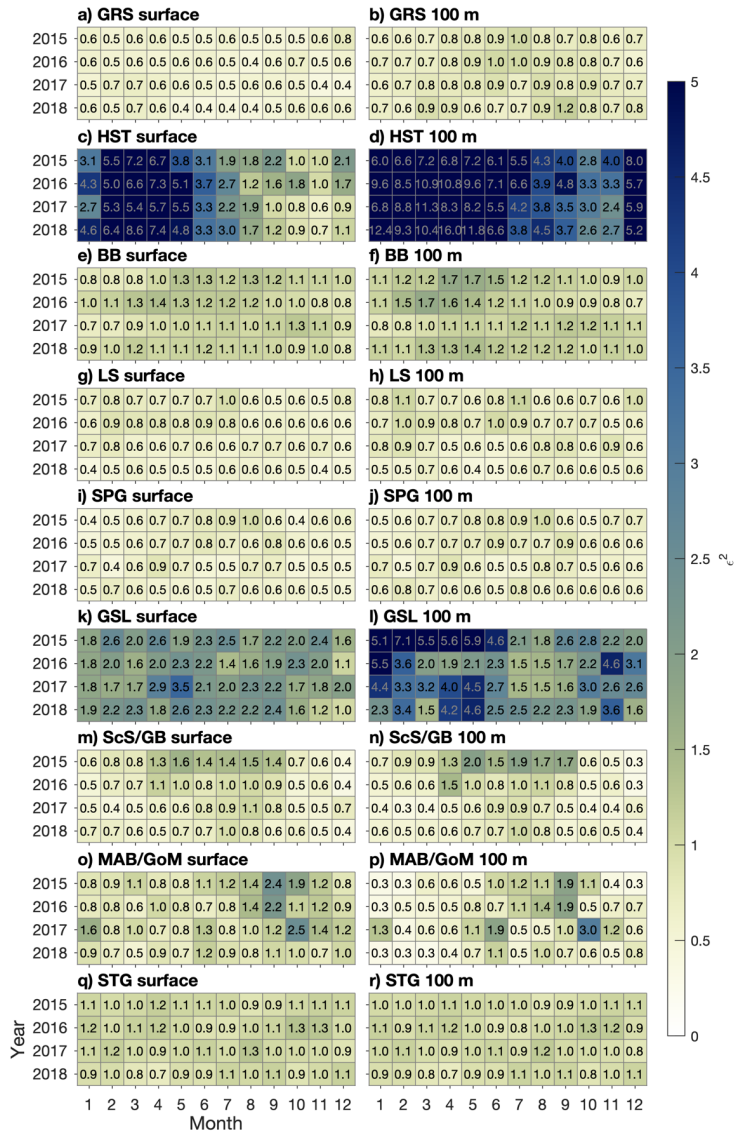
457
458
459 **Figure 8.** ε^2 of currents simulated in Ctrl, calculated for the regions shown in Fig. 1b with respect to GLORYS

460 reanalysis. See Equation 1 for the definition of ε^2.
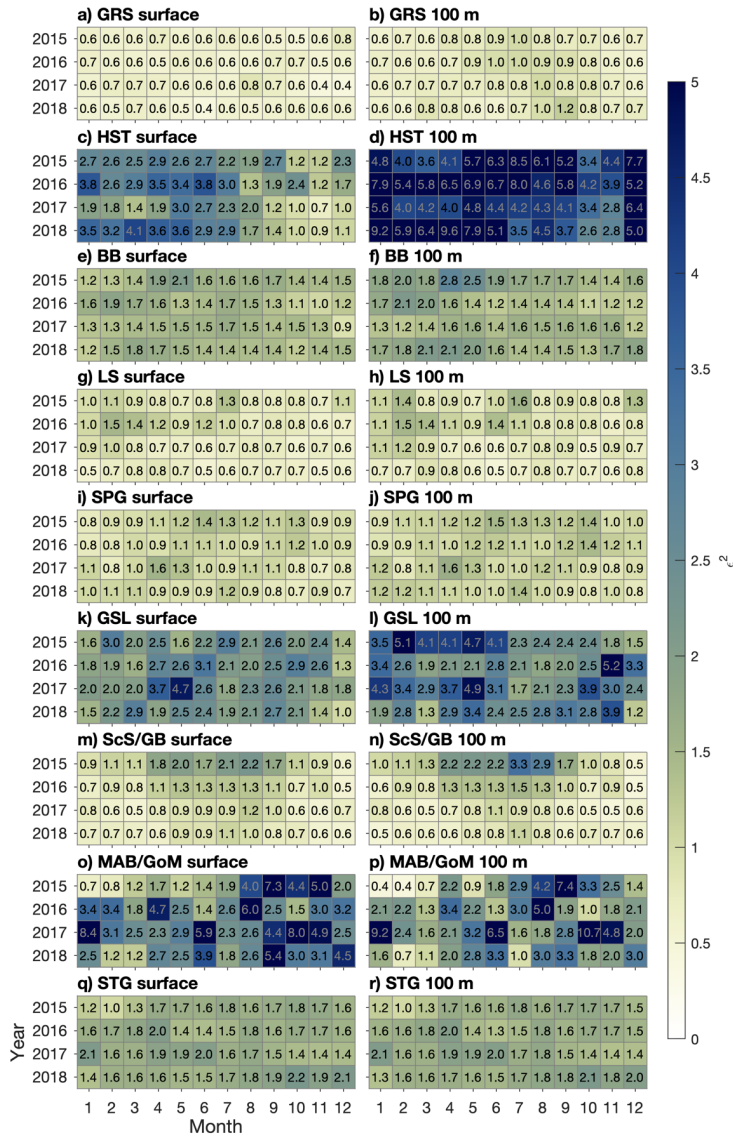
461
462
463 **Figure 9.** Similar to Fig. 8 but for currents simulated in Prog.
464

465   It should also be noted that Hudson Strait is characterized by tides of typically 3–6 m in
466   amplitude (Drinkwater, 1988). While our model includes tidal forcing, GLORYS, as stated
467   above, does not. This raises questions about how appropriate GLORYS is as a basis of evaluating
468   simulated currents in this area. Drinkwater (1988) deployed an array of current meters across
469   Hudson Strait between August and October of 1982. While exact coordinates of this array are not
470   available, the grid point in our model closest to the southwestern end of the array (station HS1)
471   can be approximated as (69.47º W, 61.15º N), with a water depth of 272 m, from Figs. 1–2 of
472   Drinkwater (1988). The eight-week average of residual current speeds at this location was
473   observed to be about 0.29 m s^{-1} and 0.12 m s^{-1} at the 30-m and 100-m depths respectively. The
474   2015–2018 average of September-mean current speeds simulated by Prog and from GLORYS at
475   the corresponding model grid point are similar to each other and somewhat less than the
476   observed value at the 30-m depth (about 0.24 m s^{-1} and 0.23 m s^{-1} respectively vs. 0.29 m s^{-1}).
477   However, at the 100-m depth, the simulated mean current speed (0.10 m s^{-1}) is more similar to
478   the observation (0.12 m s^{-1}) than the GLORYS value (0.03 m s^{-1}). Although we need to keep in
479   mind the existence of interannual variability and long-term trends which limit the conclusions we
480   can derive, these comparisons point to the possibility that the inclusion of tides in our model may
481   result in a more realistic vertical structure of currents in areas where both tides and baroclinity
482   play significant roles. The role of tides in the NWA is explored further in Sect. 4.1.

483   The temperature and salinity simulated in Prog have also been compared to observations made
484   along transects from the Atlantic Zone Monitoring Program and its off-shelf counterpart (not
485   shown). RMSE along the AR7W transect, which spans the Labrador Sea between southern
486   Labrador and southern Greenland, are largest near the surface, reaching ~2ºC for temperature
487   and ~0.5 for salinity. The errors are larger in transects across Cabot Strait and across the Scotian
488   Shelf (up to ~4ºC for temperature and ~3 for salinity), reflecting the difficulty Prog has in
489   reproducing the estuarine circulation in the Gulf of St. Lawrence and the positions of the Gulf
490   Stream and slope waters.

491   The preceding description and evaluation of the simulated circulation and hydrography have
492   highlighted two features in which the nudging of temperature and salinity in Ctrl leads to
493   improved model performance: (a) the separation of currents (the Gulf Stream and West
494   Greenland Current) from their respective coasts and (b) propagation of the low-salinity plume

496 from the St. Lawrence Estuary. Chassignet and Xu (2017) and Pennelly and Myers (2020)
497 showed respectively that increasing the horizontal resolution of their model grids from 1/12º to
498 1/50º or 1/60º resulted in more realistic representations of the Gulf Stream or the West Greenland
499 Current. Given the computational costs of making coupled physical-biogeochemical simulations
500 with a finer horizontal grid than what we currently use, a possible way to improve our modelling
501 system's performance in prognostic simulations would be to nest a finer-resolution grid covering
502 an area of particular interest (e.g., the Labrador Sea) within the existing 1/12º grid. As discussed

503 earlier, a fourth-order horizontal advection scheme with a flux limiter is a possible way to
504 improve our model's simulation of estuarine plumes in prognostic simulations.

505 **3.3 Sea ice**

506 February-mean values of sea ice cover and effective sea ice thickness (sea ice cover multiplied
507 by thickness), averaged over 2015–2018, are shown in Fig. 10. Model results from Ctrl and Prog
508 are similar in that the ice cover spans Hudson Strait and adjoining areas to its west as well as
509 most of Baffin Bay, and the thickest ice (thickness >~3.0 m) occurs along the coasts of those
510 areas. The two runs are different in that Ctrl produces more ice along the west coast of Greenland
511 and in the northwest Gulf of St. Lawrence, while Prog produces more ice along the north side of
512 Hudson Strait and on the Labrador Shelf. The larger sea ice production by Ctrl for the west coast
513 of Greenland and the northwest GSL is consistent with the lower sea-surface salinity and
514 temperature in this simulation due to the nudging (Fig. 2). For northern Hudson Strait and the
515 Labrador Shelf, a possible factor in the larger sea ice production by Prog is the fact that, in these
516 areas, offshore winds tend to cause ice divergence, which in turn leads to new ice formation
517 (Babb et al., 2021; Prinsenberg and Peterson, 1992). The cycle of open water formation,
518 freezing, and ice divergence implies changes in the surface temperature and salinity over
519 relatively small spatiotemporal scales, which could be dampened by the nudging of Ctrl to the
520 monthly CORA data set which has a horizontal resolution of 0.2°–0.5° in our study area
521 (Szekely, 2023). The role of sea ice on the physical oceanography of our study area is studied
522 further in Sect. 4.2.

523 The ice model's performance is evaluated in terms of RMSE with respect to daily AMSR2
524 (Advanced Microwave Satellite Radiometer) observations, available on a 6.5-km grid

525 (Melsheimer and Spreen, 2019). The model errors in HST, BB, and LS are generally larger in
526 Ctrl (Fig. 11) than in Prog (Fig. 12), consistent with the smaller sea ice production in these areas
527 by the former. In HST, the increase in model error during May for both runs is mostly due to
528 underestimation, indicating a too-early melting of the ice. Given that this seasonal increase in
529 model error occurs in both runs, the cause of the underestimation may be related to ice advection
530 instead of thermodynamics. Examination of sea ice budgets for areas within the NWA is a
531 possible topic of future studies.

532 **3.4 Biogeochemistry**

533 Snapshots of surface nitrate and subsurface oxygen in the Labrador Sea and surrounding areas at
534 the time of the Atlantic Zone Off-Shelf Monitoring Program (AZOMP) cruise in May 2015 are
535 shown in Fig. 13. The simulation indicates that nitrate starts to be depleted in the northern
536 Labrador Sea and along the Labrador shelf at this time but remains high in the deep central
537 Labrador Sea. Surface and shelf waters are well oxygenated and subsurface conditions along the
538 AR7W transect are characteristic of the water masses: oxygenated Labrador Sea Water
539 (depth<2000 m), lower-oxygen Northeast Atlantic Deep Water (2000–3000 m), and the more
540 oxygenated Denmark Strait Overflow Water (>3000 m), which is in line with the observations
541 along the AR7W transect (Fig. 14a). Simulated nitrate is also characteristic of the three water
542 masses (Fig. 14b). As also shown in Fig. 13, surface nitrate remains high in the central Labrador
543 Sea but is low or depleted on the West Greenland and Labrador Shelves, respectively. These
544 patterns agree with the observations. The spatial variability in alkalinity (Fig. 14c) and total
545 inorganic carbon (TIC; Figure 14d) along the AR7W transect is also well represented. The largest
546 mismatch occurs for TIC which is underestimated in the subsurface layers (depths>200 m).

547 Comparison of simulated oxygen, nitrate, alkalinity, and TIC to AZMP/AZOMP in situ
548 observations, at locations ranging from the Gulf of Maine to the Labrador Shelf, was carried out
549 for the period 2014–2018 (Fig. 15). The model simulates reasonably well the spatial and
550 temporal variability in biogeochemical variables ($0.65 < r^2 < 0.81$). Simulated oxygen has a small
551 positive bias (10.8 mmol m^{-3}, Fig. 15a) but otherwise agrees with observations. Nitrate has the
552 best match with observations ($r^2 = 0.81$) but with a small positive bias (Fig. 15b), possibly driven
553 by excess vertical mixing or by a delay in the seasonal uptake. The small bias at low TIC (i.e.,
554 surface) is likely to have the same source (Fig. 15d).
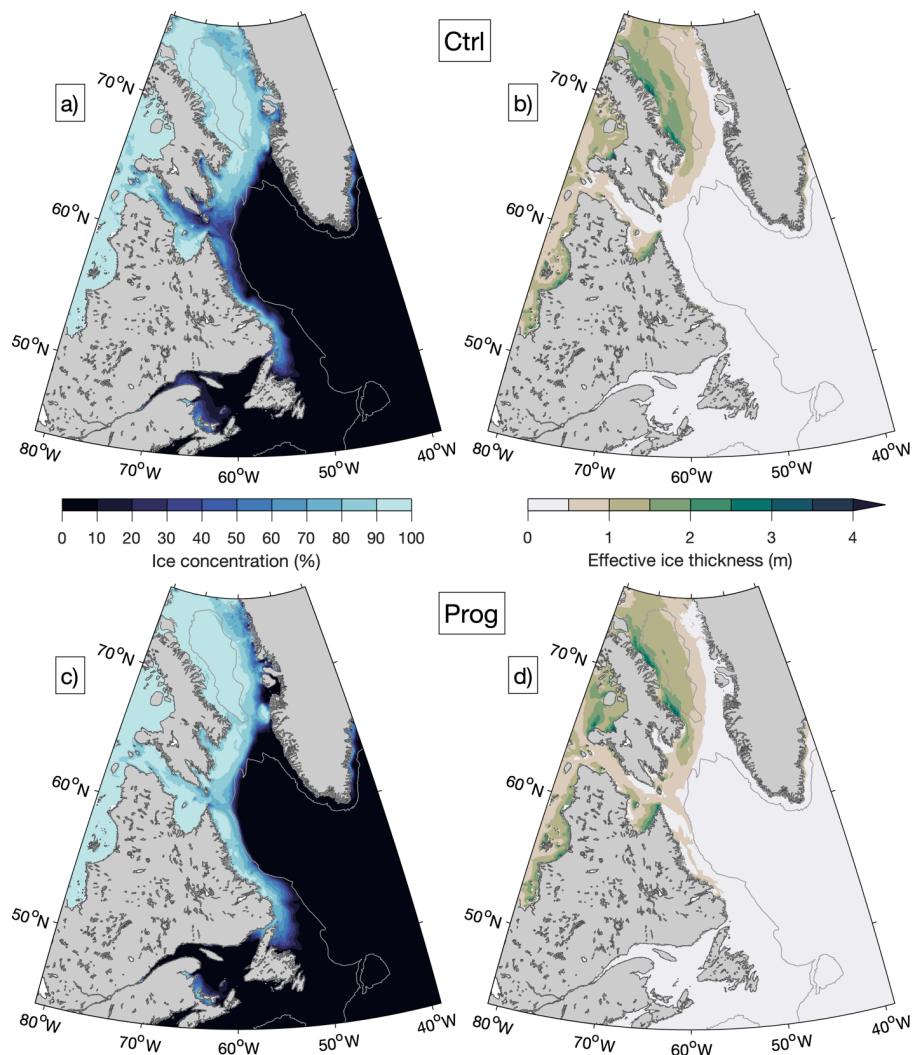
555
556
Figure 10. Monthly-mean simulated sea ice concentration **(a, c)** and effective sea ice thickness (sea ice cover

multiplied by thickness) **(b, d)** for February, averaged over 2015–2018, from Ctrl **(a, b)** and Prog **(c, d)**. The gray

contour line represents the 1000-m water depth.

560
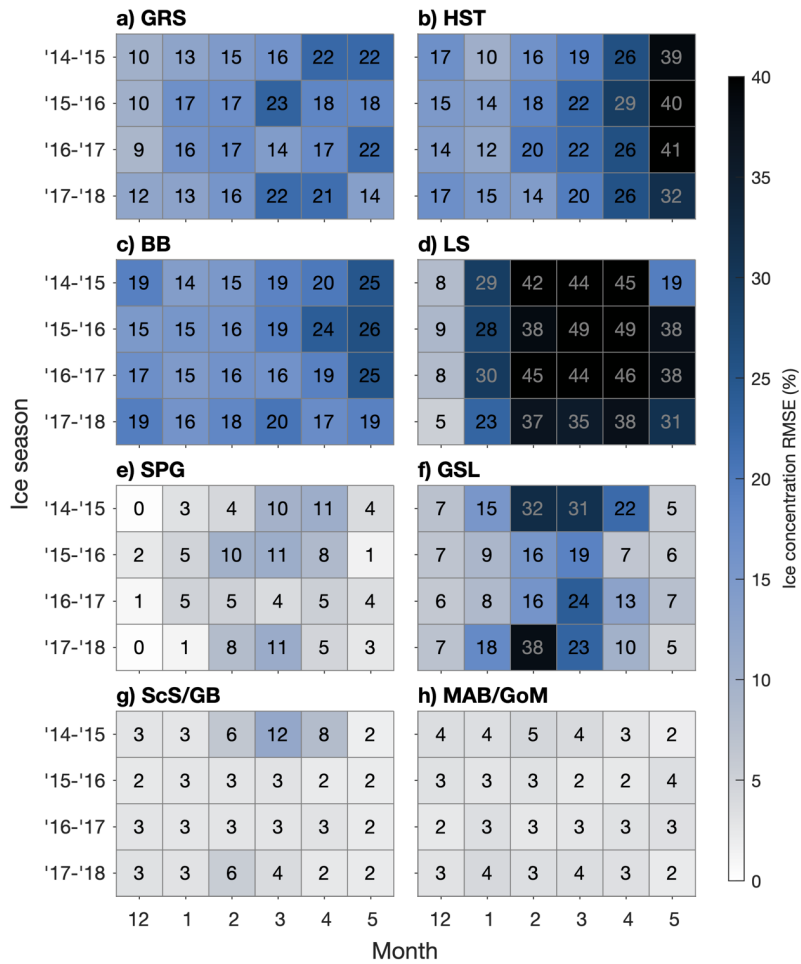
561
562
563 **Figure 11.** Root-mean-square-errors of ice concentration simulated in Ctrl, calculated for the regions shown in Fig.
564 1b with respect to AMSR2 satellite observations.
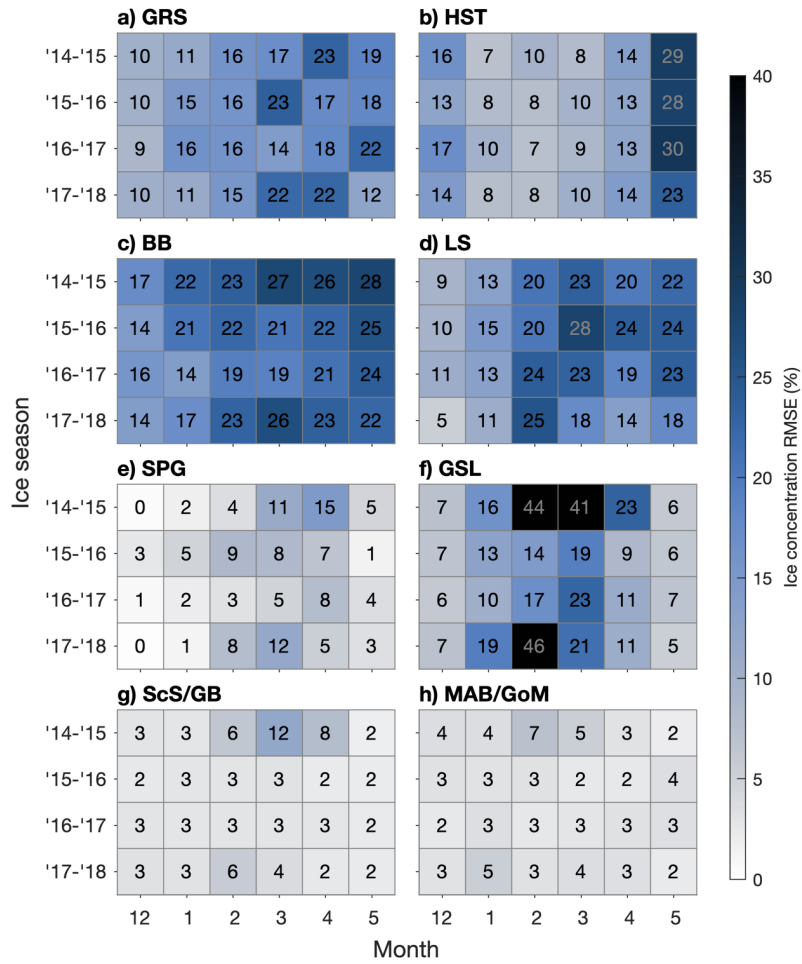
565
566
567 **Figure 12.** Similar to Fig. 11 but for ice concentration simulated in Prog.
568
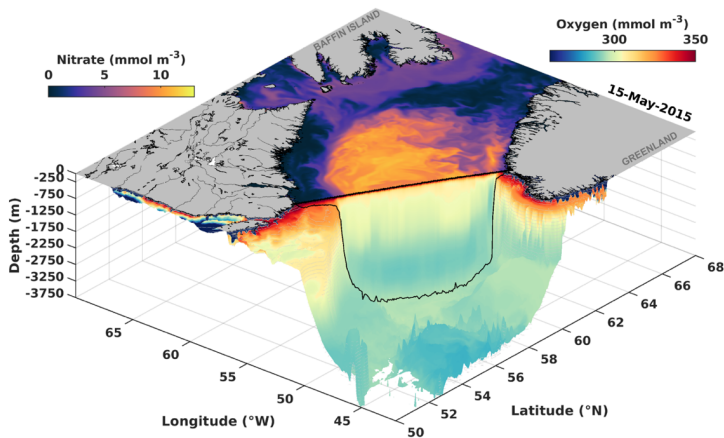
571 **Figure 13.** Three-dimensional view of simulated surface nitrate and subsurface oxygen for May 15, 2015. The thick

572 black line at the sea surface denotes the position of the AR7W transect, and the thin black line represents the model's

573 bottom topography along the transect.

574
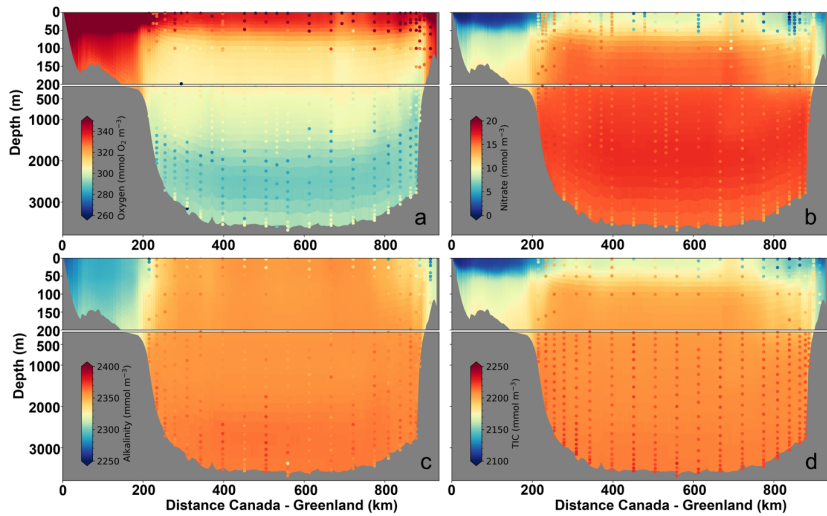
577 **Figure 14.** Comparison of simulated (background) versus observed (dots) for: oxygen **(a)**, nitrate **(b)**, alkalinity **(c)**,

578 and total inorganic carbon **(d)** during the AR7W transect in May 2015. Note: the y-axis has higher resolution in the

579 upper 200 m.
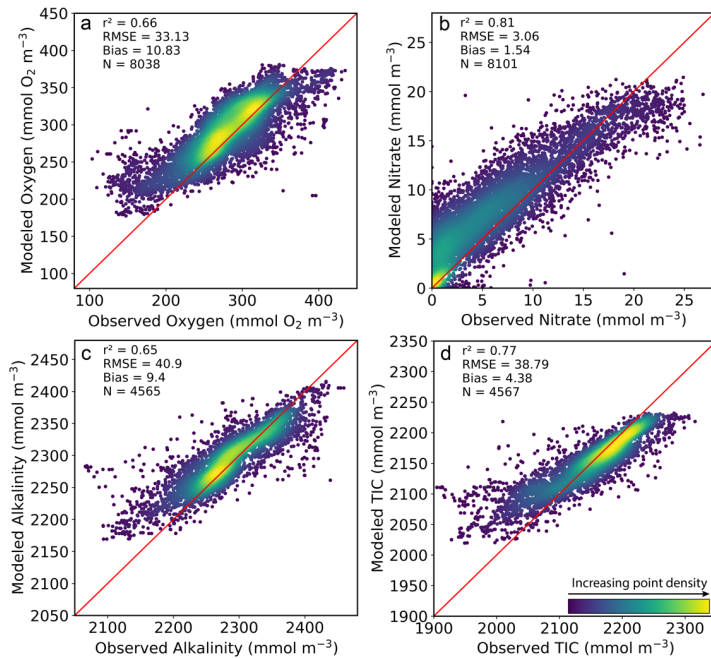
583
584
585 **Figure 15.** Comparison between simulated values and AZMP/AZOMP bottle observations during 2014–2018 for:
586 oxygen **(a)**, nitrate **(b)**, alkalinity **(c)**, and total inorganic carbon **(d)**. N is the number of observations used for the
587 comparison.
588

589 ### 3.5 Simulation of deep convection in the Labrador Sea

590 One of the important hydrodynamic features of the NWA is the occurrence of deep winter

591 convection (DWC) in the Labrador Sea and a few other areas. DWC ventilates the deep ocean,

592 contributes to the removal of anthropogenic carbon from near-surface waters, and is thought to

593 influence the larger-scale Atlantic Meridional Overturning Circulation (e.g., Rhein et al., 2011).

594 In this section, we assess the model performance in reproducing the effects of DWC at two

595 locations (indicated by numbers in Fig. 1): location 1 (54.31° W, 58.29° N) which is near the

596 centre of the "convective region" identified by Luo et al. (2014), and location 2 (50.72° W,

597 58.29° N) which is on the AR7W transect and is within the area ("Central Labrador Sea") for

619 which Yashayaev (2024, hereafter Y24) composited the available observations to form time

620 series of ocean properties from the surface to the 2000-m depth. (Location 1 is near the western

621 edge of the Central Labrador Sea as defined by Y24.) The output of Prog will be used here so

622 that the model's response to the conditions that trigger DWC can be assessed. Because the time

623 series of Y24 indicated that conditions in 2014 were markedly different from those of subsequent

624 years, the model results of 2014 will be included here even though they were excluded from the

625 preceding discussions of model performance.

626 Time series of temperature profiles at the two locations are shown in Fig. 16. The time series at

627 location 1 is generally more similar to the observation-based, area-composite time series of Y24

628 (his Fig. 3) than at location 2. This is consistent with the fact that location 1 is at the centre of the

629 area where DWC occurred in the modelling study of Luo et al. (2014), which they found to agree

630 with areas of convection observed by, e.g., Lavender et al. (2000). The time series of simulated

631 temperature profiles at location 1 includes several features that appear in Y24, such as: 1) the

632 turbulent vertical mixing/convection being much stronger in 2015 than in 2014, with the 3.4°C

633 contour of simulated temperatures extending down to the ~1600-m depth in 2015 but just to the

634 ~1000-m depth in 2014; 2) temperatures below 3°C occurring from the surface to the ~200-m

635 depth from late 2015 to early 2016; and 3) temperatures above 6°C extending to a maximum of

636 ~100 m below the surface during the summer. Given that: 1) our model does not directly

637 simulate or parameterize deep convection and 2) we are comparing the temporal evolution of

638 simulated temperatures at one location against a composite of observations over an area with a

639 diameter of O(100 km) in Y24, we find these similarities encouraging.

640 It should be noted that the horizontal grid size of our model is O(1 km), which is much coarser

641 than the typical horizontal scale of O(100 m) for the convective plumes (e.g., The Lab Sea

642 Group, 1998). Furthermore, our circulation model does not use an explicit winter advection

643 scheme, instead it uses large vertical mixing coefficients produced by the modified "2.5-level"

644 scheme of Mellor and Yamada (1982) to mimic the intense convective mixing associated with

645 DWC. A fine-resolution model with a horizontal grid size of O(100 m) nested within

646 DALROMS-NWA12 v1.0 will be used in our future research to develop better parameterizations

647 of DWC over the NWA and to examine how the model simulates deep ocean ventilation and

648 near-surface carbon removal due to DWC.

Figure 16. Daily-mean simulated temperatures from Prog, vertically interpolated to 5-m depth intervals between the 0- and 2000-m depths, at location 1 (54.31° W, 58.29° N) **(a)** and location 2 (50.72° W, 58.29° N) **(b)**, indicated as "1" and "2" respectively in Fig. 1. Major tick marks correspond to 1 January of each year and minor tick marks correspond to the first days of February–November. Temperature values between 6°C and 11°C are shown with black contour lines at 1°C intervals.

4 Sensitivity studies

The ocean circulation and sea ice modules of DalROMS-NWA12 v1.0 are used in this section to examine the roles of tides and sea ice in the hydrodynamics of the NWA. This is done by comparing the model results from Prog to those from two additional simulations that are identical to Prog but with the tidal forcing absent from one (NoTides) and sea ice absent from the other (NoIce). In NoIce, the net surface heat flux is set to zero if it would cool the ocean and the sea surface temperature is already at or below the local freezing temperature. The difference

683 between surface temperatures simulated in Prog and in NoTides (Prog minus NoTides) will be

684 denoted ΔT_{sfc}^{P-NT} and the difference in bottom temperatures will be denoted ΔT_{btm}^{P-NT}. Similar

685 notations will be used for differences in salinity (e.g., ΔS_{sfc}^{P-NT}) and current speed (e.g.,

686 $\Delta|V|_{sfc}^{P-NT}$) and for differences between model results from Prog and NoIce (e.g., ΔT_{sfc}^{P-NI}).

4.1 The effect of tides

688 Differences between Prog and NoTides (Prog minus NoTides) in sea surface salinity, currents,

689 and temperature over Baffin Bay and the Labrador Sea, averaged over the winters (December–

690 February) and summers (June–August) of December 2014–August 2018, are shown in Fig. 17. In

691 winter (Fig. 17a–b), differences between the simulations of temperature and salinity over this

692 area are relatively small – generally within ±1 for salinity, and up to ~+1.5°C for temperature. In

693 summer (Fig. 17c–d), ΔS_{sfc}^{P-NT} is positive along most of the Baffin Island coast, in Ungava Bay,

694 and on the northern Labrador Shelf (up to ~7 in Ungava Bay) while ΔT_{sfc}^{P-NT} is mostly negative

695 throughout the area but especially over shelves (~-1.0°C). These differences between Prog and

696 NoTides are consistent with the presence of sea ice over large portions of this area during winter,

697 given that sea ice can modulate tidal mixing and thus tend to reduce the differences between the

698 ocean states simulated with and without tides. In summer, the presence of tidal mixing in Prog

699 contributes to vertical mixing over shelf areas, resulting in surface waters that are saltier and

700 colder than if there were no tides and the water column were more highly stratified. There are,

701 however, areas in which the inclusion of tides results in positive ΔT_{sfc}^{P-NT} during the summer,

702 notably along the coast of Ungava Bay. Given that ΔS_{sfc}^{P-NT} is positive throughout the Bay, the

703 contrast between positive ΔT_{sfc}^{P-NT} along the coast and negative ΔT_{sfc}^{P-NT} near the Bay's mouth

704 suggests air-sea fluxes might differ between the two parts of the Bay.

705 The effect of tides on water temperature within Ungava Bay is explored in Figs. 18 and 19. In

706 winter, the models results from Prog and NoTides are similar not only in terms of the surface

707 temperature (Fig. 18a), but also in terms of bottom temperature ($|\Delta T_{btm}^{P-NT}| <\sim 1.0$°C, Fig. 18b)

708 and current speeds at both the surface and bottom ($\Delta|V|_{sfc}^{P-NT}$ and $\Delta|V|_{btm}^{P-NT} <\sim 0.1$ m s^{-1}, Fig.

709 18a–b). In summer at the sea surface (Fig. 18c), both $\Delta|V|_{sfc}^{P-NT}$ and ΔT_{sfc}^{P-NT} are positive along

the coast but generally negative in the outer bay. Along the bottom in summer (Fig. 18d), ΔT_{btm}^{P-NT} is positive and as large as ~+4°C along the coast, while in the outer bay ΔT_{btm}^{P-NT} is small ($|\Delta T_{btm}^{P-NT}| < $~1.0°C) and the currents are generally weak in both simulations. The patterns of mean summer sea ice concentration are also different between the two simulations, with the ice cover produced in Prog (Fig. 19a) being highest over the outer bay (up to ~40%) and low near the coast, while NoTides (Fig. 19b) produces a wide area of high ice cover along the coast (up to ~90%). The patterns of mean summer sea surface temperature from the two simulations (Fig. 19c–d) correspond to those of the sea ice cover, with areas of higher (lower) ice cover corresponding to lower (higher) temperatures. Given that the only difference between the Prog and NoTides simulations is the inclusion of tides in the former, these results suggest that tides along the coast of Ungava Bay promotes an earlier disappearance of ice there during the summer, and this in turn leads to a larger flux of solar radiation into the ocean and a less impeded flow.

The effect of tides is also evident in the region surrounding two other areas with large tidal ranges, the St. Lawrence Estuary and the Bay of Fundy. In both winter and summer, ΔS_{sfc}^{P-NT} in the St. Lawrence Estuary (Fig. 20a,c) is positive (up to ~6.0 in most of the Estuary but >10 in parts of the Upper Estuary during the summer), suggesting that tidal mixing brings higher-salinity subsurface water towards the surface. In summer (Fig. 20c), the influence of this higher salinity due to tidal mixing spreads into the northwest Gulf of St. Lawrence due to the propagation of the estuarine plume. In the Bay of Fundy, the salinity difference is also positive in both seasons. In winter, ΔS_{sfc}^{P-NT} ranges from ~0.4 in most of the Bay to ~2.4 near the Saint John River's mouth and in summer, it ranges from ~1.2 in the upper Bay to ~3.6 near the Saint John River's mouth. The role of tidal mixing is also evident in the patterns of sea surface temperatures (Fig. 20b,d), with ΔT_{sfc}^{P-NT} positive in winter (up to ~1.5°C in both the St. Lawrence Estuary and the Bay of Fundy) and negative in summer (as low as ~-4.5°C in both areas). Differences between the simulations are also visible over the open ocean for all three fields. As Wang et al. (2020) have suggested, this may be caused by internal tides that are generated near the shelf break and propagate offshore.
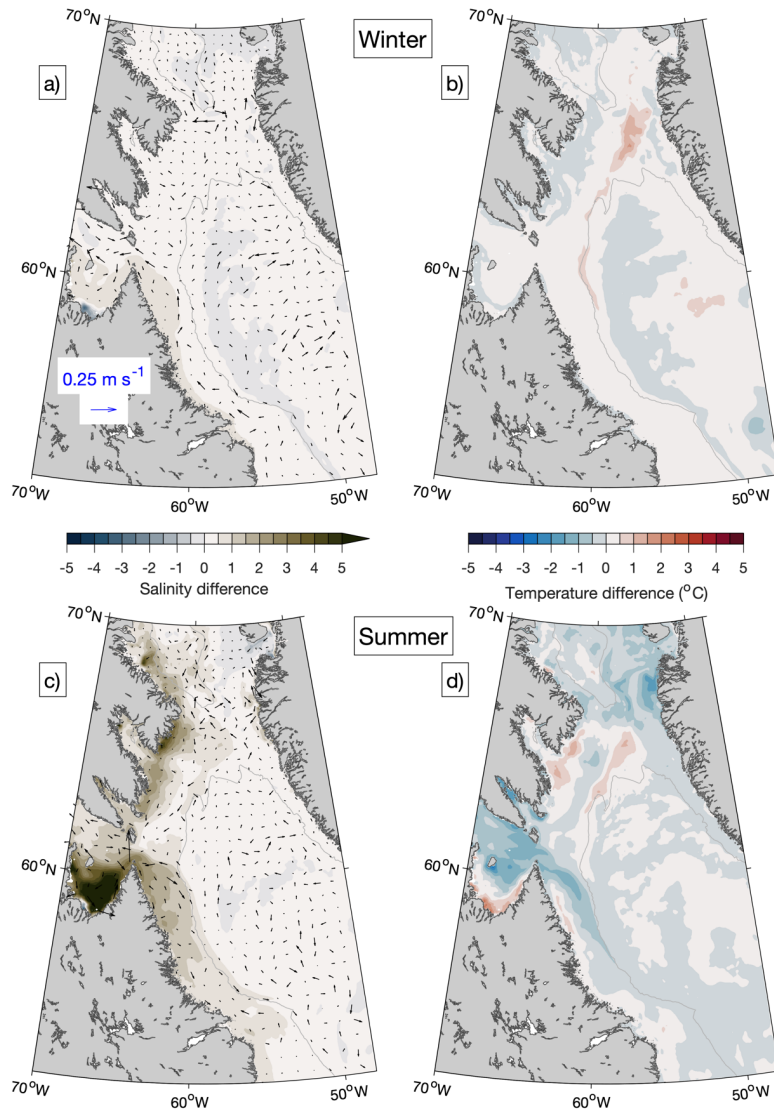
753
754
755 Figure 17. Differences in seasonal-mean simulated sea surface salinity and currents **(a, c)** and temperature **(b, d)**

756 over Baffin Bay and the Labrador Sea when model results from NoTides are subtracted from those from Prog,

757 averaged over winters **(a, b)** and summers **(c, d)** of 2015–2018. Difference vectors are shown at every 12th model

758 grid point. The gray contour line represents the 1000-m water depth.
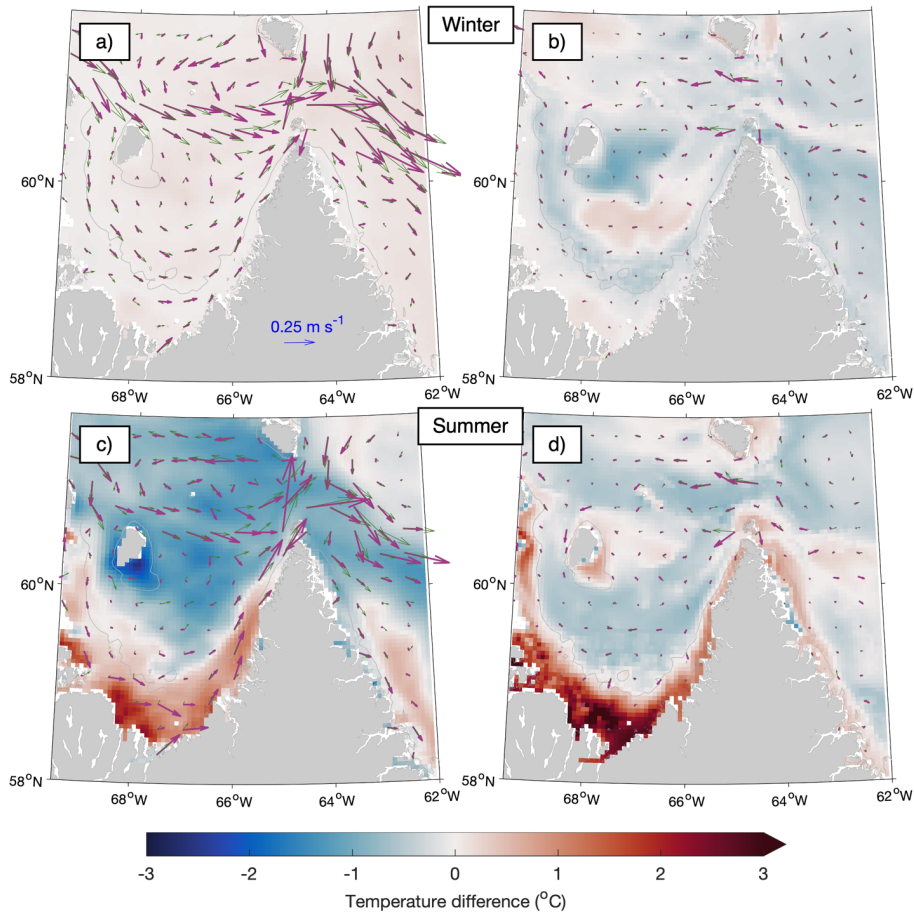
761
762
763 **Figure 18.** Differences between Prog and NoTides over Ungava Bay: 2015–2018 averages of seasonal-mean

764 simulated currents (thick magenta arrows: Prog, thin green arrows: NoTides) and temperature difference (Prog

765 minus NoTides) at the sea surface **(a, c)** and bottom layer **(b, d)** in winter **(a–b)** and summer **(c–d)**. Current vectors

766 are shown at every sixth model grid point. The gray contour line represents the 100-m water depth.
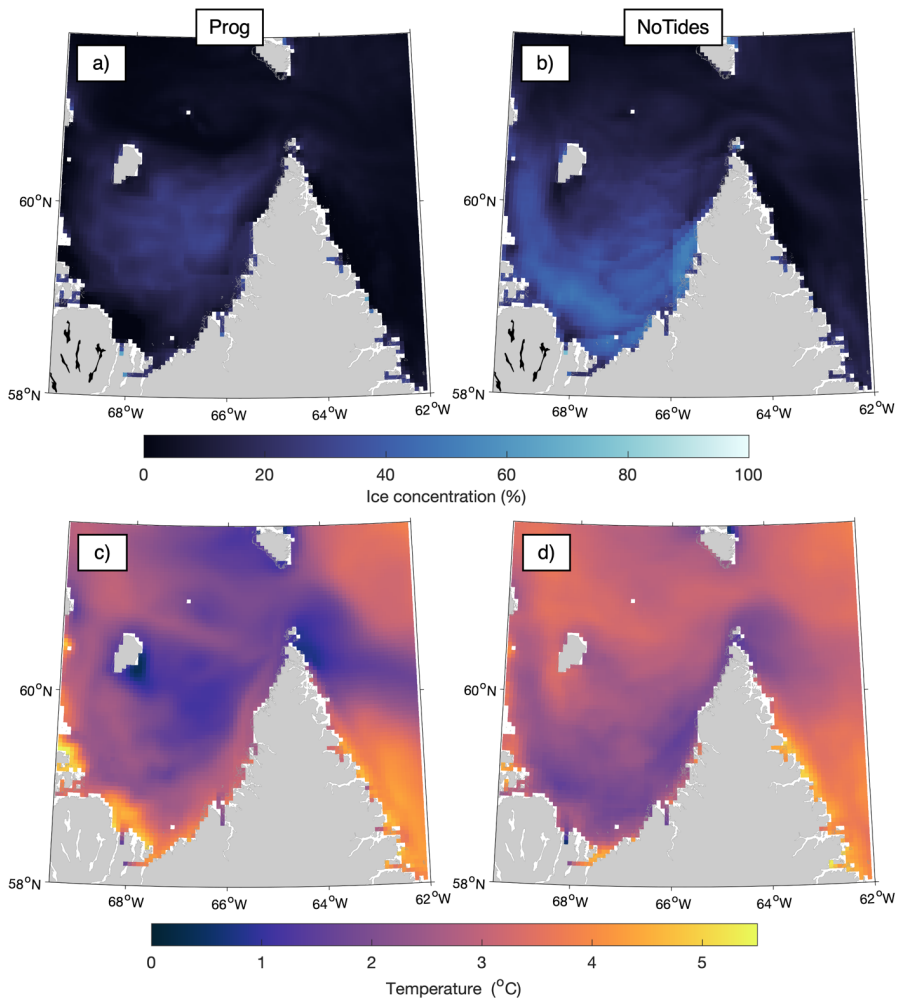
768
769
770
771 **Figure 19.** 2015–2018 averages of seasonal-mean sea ice concentrations in Ungava Bay during summer simulated

772 in runs Prog **(a)** and NoTides **(b)**; seasonal-mean sea surface temperature for summer simulated by runs Prog **(c)** and

773 NoTides **(d)**.
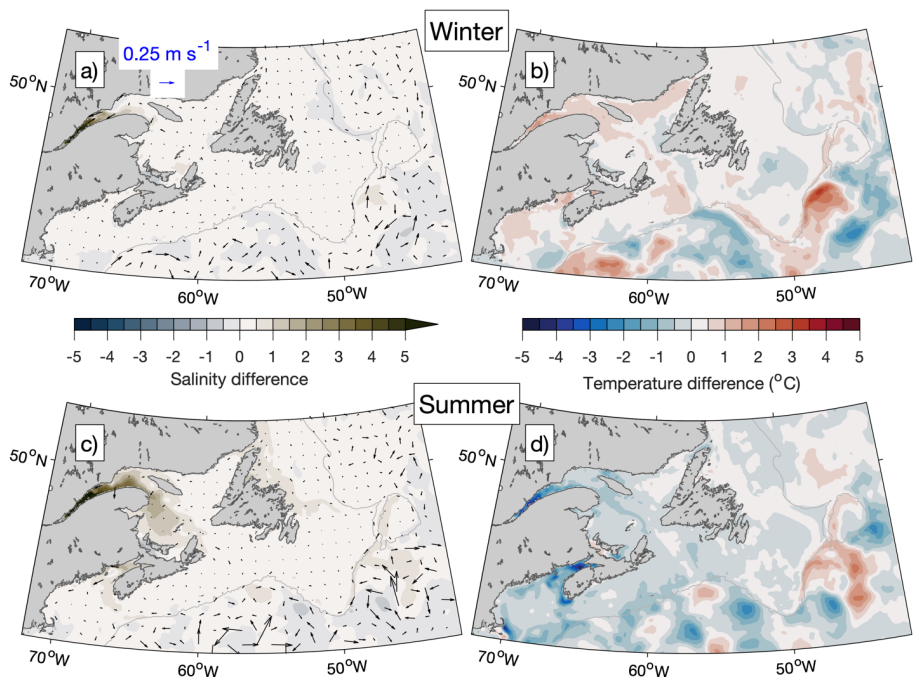
777   **Figure 20.** Similar to Fig. 18, but for the area between the Gulf of Maine and the southern Labrador Sea.

Deleted: 19

Deleted: 7

778   **4.2 The effect of sea ice**

779   The effect of sea ice is examined next by comparing simulated surface fields from Prog to those

780   from the simulation in which ROMS is run without coupling to CICE (NoIce). A prominent

781   feature in winter is the horizontal gradient in ΔS_{sfc}^{P-NI}, approximately aligned with the 1000-m

782   isobath, in western Baffin Bay (Fig. 21a). ΔS_{sfc}^{P-NI} is positive on the shelf (~0.2) but negative

Deleted: 0

783   offshore of the shelf break (~-0.3). In the zone where ΔS_{sfc}^{P-NI} changes signs, $\Delta \left|\vec{V}\right|_{sfc}^{P-NI}$ is positive

784   (up to ~0.3 m s^{-1}). The area on the shelf where ΔS_{sfc}^{P-NI} is positive coincides with the highest

785   average sea ice thickness in the domain (Fig. 10d), which makes the higher salinity in Prog

786   consistent with brine rejection at the time of sea ice formation. Values of $\left|\Delta T_{sfc}^{P-NI}\right|$ in winter (Fig.

787   21b) tend to be largest over the parts of Baffin Bay and the northern Labrador Shelf where the

Deleted: 0

792 ice edge occurs in Prog (Fig. 10c). ΔT_{sfc}^{P-NI} in these areas are negative (as low as ~-1.9°). Surface

793 heat flux is expected to result in positive ΔT_{sfc}^{P-NI}, given that in winter it is expected to cool the

794 ocean surface while sea ice can insulate the ocean surface below from cold air. Another possible

795 factor in ΔT_{sfc}^{P-NI} is vertical mixing, which is examined later.

796 In summer, ΔS_{sfc}^{P-NI} and ΔT_{sfc}^{P-NI} (Fig. 21c and 21d respectively) are lowest in western Baffin Bay,

797 with the former as low as ~-4.0 psu (reflecting the input of freshwater due to melting sea ice) and

798 the latter as low as ~-4.7°C (reflecting the blocking of shortwave radiation by the sea ice that

799 remains in summer). These results suggest that, as sea ice in areas such as Baffin Bay and the

800 Labrador Shelf decline in a warming climate, areas downstream from them such as the Scotian

801 Shelf and the Gulf of Maine will experience changes in the temperature and salinity of the water

802 that is brought there by the Labrador Current. The effect of changes in water masses advected

803 into a given area, in combination with changes that occur in situ due to climate change, is

804 another possible topic of future research.

805 Differences in the wintertime vertical stratification and vertical mixing between Prog and NoIce

806 are examined further using vertical profiles of four-year mean wintertime temperature, salinity,

807 and vertical eddy viscosity produced by the two runs, as well as the squared buoyancy frequency

808 (N^2) calculated from the mean wintertime temperature and salinity using the Gibbs-SeaWater

809 Oceanographic Toolbox (McDougall and Barker, 2011). The profiles represent temporal averages

810 over the same period as in Figs. 21a–b (winters of 2015–2018) and are calculated at 1-m depth

811 intervals for two locations: location A (62.56° W, 67.60° N), indicated by the square in Fig. 21b,

812 where ΔT_{sfc}^{P-NI} is small and the 2015–2018 mean of the February-mean sea ice cover is ~95%

813 (Fig. 10c), and location B (57.64° W, 67.60° N), indicated by the circle in Fig. 21b, where

814 ΔT_{sfc}^{P-NI} has a large magnitude (~-1.9°C) and the four-year mean of the February-mean sea ice

815 cover is ~84%. The model's water depths at the two locations are similar (231 m and 218 m).

816 The vertical profiles of mean wintertime temperature (Fig. 22a) and salinity (Fig. 22b) at location

817 A are similar between runs Prog and NoIce, with a vertical range of <1.4°C for temperature and

818 <0.8 for salinity in both runs. The profiles of N^2 (Fig. 22c) are thus also similar between the runs,

819 with maximum values of ~6 × 10⁻⁵ s⁻² about 40 m below the sea surface. Negative values of N^2,

820 indicating instability, are limited to the top few metres of the water column. Values of the

831   Richardson number (not shown) below 0.25, including negative values, are limited to the top 5 m

832   of the water column, again indicating a mostly stable water column and weak convection in both

833   Prog and NoIce. The mean wintertime vertical mixing below the surface is very weak in both

834   runs (Fig. 22d), with the vertical eddy diffusivity from both runs having maximum values of

835   ~0.02 m^2 s^{-1} about 10 m below the surface and having values <0.002 m^2 s^{-1} in ~80% of the water

836   column. It should be noted that the mean wintertime stress exerted on the sea surface (by winds

837   and/or sea ice in Prog and by winds in NoIce) differs significantly between the two runs (Fig.

838   22d). The surface stress has a much smaller magnitude in Prog (0.02 N m^{-2}) than in NoIce (1.0 N

839   m^{-2}), which can be explained by the buffering effect of sea ice on the wind stress in Prog. Due to

840   this buffering effect of sea ice, the wind-induced vertical mixing in the surface layer (Fig. 22d) is

841   weaker in Prog than in NoIce, as expected.

842   In contrast to location A, the vertical profiles of mean wintertime model results at location B

843   differ significantly between runs Prog and NoIce. The mean wintertime temperature (Fig. 23a)

844   has a vertical range of >3°C in Prog (about -0.9°C near the surface and 2.4°C near the bottom)

845   but <1.0°C in NoIce (about 1.1°C near the surface and 1.7°C near the bottom). The mean

846   wintertime salinity (Fig. 23b) has a vertical range of ~0.5 in Prog (about 34.0 near the surface

847   and 34.5 near the bottom) but just ~0.1 in NoIce (about 34.5 near the surface and 34.6 near the

848   bottom). Values of N^2 (Fig. 23c) from both runs are lower than at location A; with a maximum of

849   ~1.9 × 10^{-5} s^{-2} in Prog and ~2.1 × 10^{-6} s^{-2} in NoIce. In addition, the N^2 in NoIce is negative in the

850   top ~20 m of the water column and between depths of ~40 and ~50 m, indicating unstable

851   stratification and unrealistically strong convection. The Richardson number is <0.25 in the top ~5

852   m of the water column in Prog, and at approximately the same depths as the negative values of

853   N^2 in NoIce. The maximum vertical eddy diffusivity coefficient is ~0.3 m^2 s^{-1} in NoIce, which is

854   much larger than the maximum values of ~0.06 m^2 s^{-1} in Prog, while the surface stress is similar

855   at ~0.1 N m^{-2} in both runs.

856   A possible explanation for the relatively warm (>2.0°C) and salty (>34.0 psu) subsurface water

857   in the lower water column at location B in Prog (solid blue lines in Fig. 23a,b) is the horizontal

858   advection of relatively warm and salty waters from the south to this location. In Prog, the ocean-

859   to-air heat flux in winter results in cooling of the near-surface water as well as sea ice formation,

860   and subsurface ablation of the sea ice can be a source of fresh water that contributes to vertical

Deleted: 1

Deleted: 1

Deleted: 1

Deleted: 2

Deleted: 2

Deleted: 2

Deleted: 2

870 **Figure 21.** Differences in seasonal-mean simulated sea surface salinity and currents **(a, c)** and temperature **(b, d)**

871 over Baffin Bay and the Labrador Sea when results of NoIce are subtracted from those of Prog, averaged over

872 winters **(a, b)** and summers **(c, d)** of 2015–2018. Difference vectors are shown at every 12th model grid point. The

873 gray contour line represents the 1000-m water depth. Locations A and B, for which the vertical profiles of model

874 variables are shown in Figs. 22 and 23, are indicated in panel **(b)** with a square and a circle respectively.

Deleted: 0

Deleted: (psu)

Deleted: 1

Deleted: 2
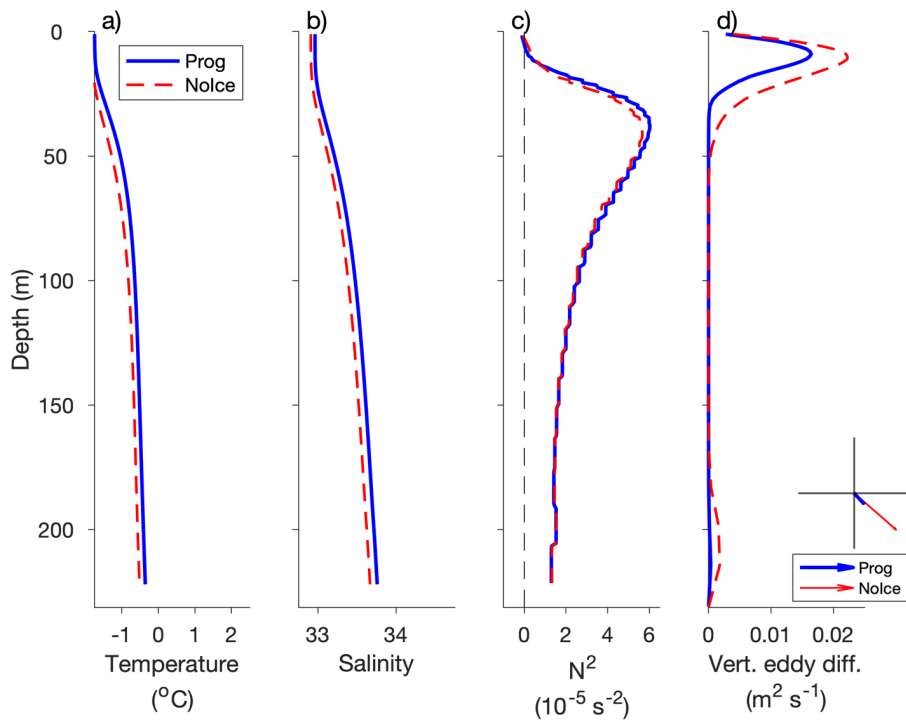
879
880
881 **Figure 22.** Vertical profiles of wintertime temperature (**a**), salinity (**b**), squared buoyancy frequency (**c**), and vertical

882 eddy diffusivity (**d**) simulated by the model in Prog (blue solid line) and NoIce (red dashed line), averaged over

883 2015–2018, interpolated to 1-m depth intervals, at location A, indicated by the square in Fig. 21b (62.56° W, 67.60°

884 N). Also shown in panel (**d**) is the stress exerted on the sea surface by sea ice and/or winds in the Prog (thick arrow)

885 and NoIce (thin arrow) runs, averaged over the same period as the other fields. The x- and y-axes for the surface

886 stress range from -0.1 to 0.1 N m^{-2}.

Deleted: 1

Deleted: 0

889
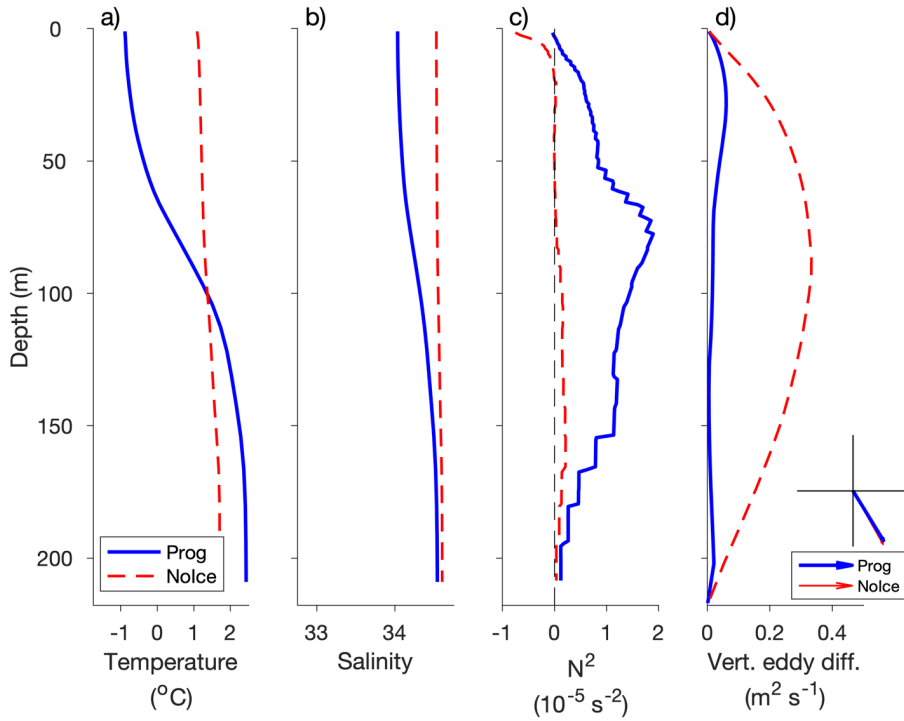
890
891

892 **Figure 23.** Similar to Fig. 22, but for location B, indicated by the circle in Fig. 21b (57.64° W, 67.60° N). Note the
893 change from Fig. 22 in the x-axis limits for the squared buoyancy frequency (**c**) and the vertical eddy diffusivity (**d**).

Deleted: 2
Deleted: 1
Deleted: 0
Deleted: 1
Formatted: Tab stops: Not at 5 cm

894 stability. The advection of relatively warm, salty subsurface waters from the south would also
895 occur in NoIce, but in this case the near-surface water would be cooled to the freezing point
896 without an accompanying reduction in salinity, which may explain the very large vertical mixing
897 and nearly uniform vertical profiles of temperature and salinity in this run.

Deleted: ¶

898 **5 Conclusions**

899 In this study, a newly-developed, fully-coupled modelling system for simulating the ocean
900 circulation, sea ice, and biogeochemistry of the northwest North Atlantic Ocean (DalROMS-

906   NWA12 v1.0) was described. The model domain covers the area from Cape Hatteras to Baffin
907   Bay with a horizontal resolution of ~2 to ~8 km, making this modelling system highly suitable
908   for a range of research topics, including study of the biological carbon pump and quantification
909   of the major physical and biogeochemical (BGC) processes influencing the ocean carbon cycle
910   over the region. The results of two simulations using this modelling system, with and without
911   nudging of the simulated temperature and salinity towards a blend of observations and
912   reanalysis, were compared to observations and reanalysis. We found that results of the control
913   run, which included the nudging, are more realistic than results of the prognostic (un-nudged)
914   simulation for several important physical features observed in this region, such as separation of
915   the Gulf Stream and the West Greenland Current from their respective coasts, as well as
916   propagation of low-salinity waters from the St. Lawrence Estuary. These results demonstrate the
917   utility of simple data assimilation in reducing the systematic model errors that can be attributed
918   to model configuration (such as horizontal grid resolution in the case of currents' separation from
919   coasts and the choice of tracer advection scheme in the case of estuarine plume propagation) and
920   unresolved or parameterized physical and BGC processes. The prognostic simulation, while
921   having difficulties with the above-mentioned features, was able to reproduce the general
922   spatiotemporal patterns of the physical fields and outperformed the control run in terms of the
923   sea ice concentration. The major differences between the simulations in the sea ice extent
924   highlight the complex nature of interactions among the atmosphere, ocean, and sea ice.

925   The modelling system was able to reproduce the general patterns of BGC variables over the
926   northwest Atlantic shelves and in the Labrador Sea. Further validation will include comparisons
927   with observations made by BGC Argo floats (Johnson and Claustre, 2016). Future work will use
928   this modelling system to investigate the biological carbon pump in the Labrador Sea including
929   vertical flux estimates derived from BGC Argo (Wang and Fennel, 2022 and 2023). The addition
930   of silicate as a state variable will also be tested.

931   As an example of application of this modelling system, sensitivity studies were made in which
932   results of the prognostic simulation were compared to those from similar simulations from which
933   either the tides or simulation of sea ice were excluded. The comparisons suggest that tides and
934   sea ice strongly affect the physical oceanography of the NWA in several ways. These include the

935 combined effects of tides and sea ice (in Ungava Bay) as well as individual effects (e.g., higher
936 surface salinity in summer when sea ice is not simulated).

937 In addition to studies of the biological carbon pump and of the downstream effects of changes in
938 the water transported by the Labrador Current, another possible direction of future research is to
939 explore further the effects of model configuration, such as parameterization of deep convection
940 or the choice of advection schemes (including the use of non-zero horizontal eddy diffusivity and
941 viscosity with the third-order upstream scheme). In addition, we can use the ocean state
942 simulated by this model as input for numerical particle-tracking experiments to investigate
943 connectivity among different areas of the NWA. The resulting metrics of connectivity under
944 current and projected future climate conditions can support decision-making processes
945 concerning conservation measures. The model will also be used to compare approaches to
946 reducing bias in long-term simulations (Renkl et al., in prep.).

947 The high air-to-sea flux of CO_2 and the subsequent downward export of fixed carbon make the
948 NWA a key component in the global climate system, but it is a remote region where seasonal
949 transitions can take place in just a few weeks (e.g., in terms of pCO_2; Körtzinger et al., 2008) and
950 details of the interactions between physical and biogeochemical processes are still unknown or
951 remain poorly integrated into models (e.g., the sea-ice carbon pump; Richaud et al., 2023). The
952 four-dimensional ocean states produced by numerical models can aid in the interpretation of
953 observations as well as enable experiments that elucidate the roles of various processes in the
954 ocean and how those processes might change under future climate scenarios. As part of our
955 future studies, this advanced coupled modelling system will be run for longer simulation periods
956 to examine the effects of climate change on the marine conditions over the NWA. The modelling
957 system will also be used to predict the temporal and spatial variability of future marine
958 conditions over the region under different climate scenarios.

959 **Appendix A: The vertical coordinate system in ROMS**

960 ROMS uses a generalized terrain-following vertical coordinate system with several options
961 for vertical transformation equations and vertical stretching functions. In this study the default
962 configuration is used, with the vertical coordinate S defined as (Hedstrom, 2018):

963
$$z(x,y,\sigma,t) = \zeta(x,y,t) + [\zeta(x,y,t) + h(x,y)]S(x,y,\sigma) \tag{A1}$$

964 $$S_(x, y, \sigma) = \frac{h_c + h(x,y)C(\sigma)}{h_c + h(x,y)}$$ (A2)

965 $$C_(\sigma) = \frac{\exp(\theta_B C'(\sigma) - 1)}{1 - \exp(-\theta_B)}$$ (A3)

966 $$C'_(\sigma) = \frac{1 - \cosh(\theta_S \sigma)}{\cosh(\theta_S) - 1}$$ (A4)

967 where σ ranges from 0 at the free surface to -1 at the ocean bottom, ζ is the free surface, h is the

968 undisturbed water column thickness, h_c is the value of h below which the vertical layers are more

969 uniformly spaced, and θ_s and θ_b are parameters that control the vertical resolution near the

970 surface and the bottom respectively. In this study ROMS has 40 layers and the parameters h_c, θ_s,

971 and θ_b are set to 100 m, 5.0, and 0.5 respectively.

972 **Appendix B: Seasonal-mean simulated fields**

973   Seasonal means of salinity and currents in Baffin Bay and the northern Labrador Sea

974 simulated in Ctrl and Prog, averaged over the period December 2014–December 2018, are

975 shown in Figs. B1 and B2. Differences between the simulations are more evident in summer

976 (June–August; Figs. B1c–d and B2c–d than in winter (December–February; Figs. B1a–b and

977 B2a–b). The northward branch of the West Greenland Current and the Baffin Island Current are

978 stronger in Prog by up to ~0.25 m s^{-1} at the surface and ~0.15 m s^{-1} for model results interpolated

979 to the 100-m depth. In the area between the southern Labrador Sea and the Gulf of Maine (Figs.

980 B3 and B4), the difference in salinity between the simulations is more prominent in summer,

981 following the annual peak in freshwater discharges from the St. Lawrence and other rivers. In the

982 St. Lawrence Estuary, the 2015–2018 mean of summer surface salinity simulated in Prog is

983 lower than that from Ctrl by up to ~3.5, but further downstream in the Gulf of St. Lawrence, the

984 salinity from Prog is higher by ~2.
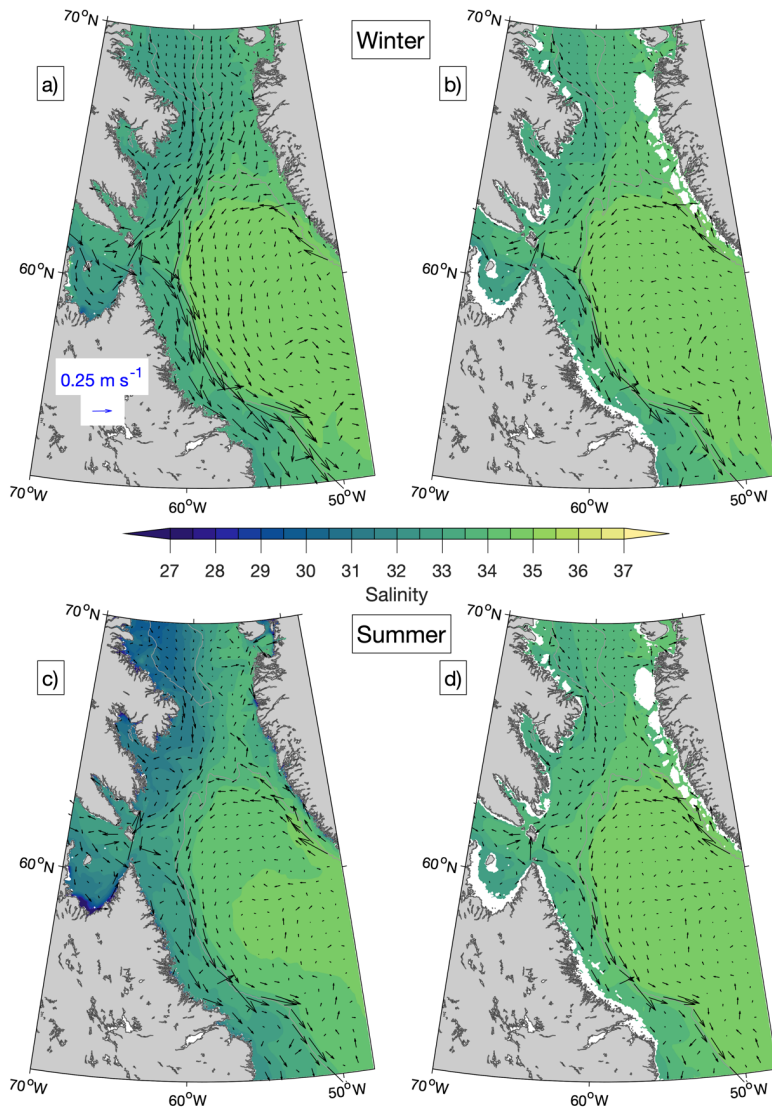
985
986
987 **Figure B1.** Seasonal-mean simulated salinity and currents at the sea surface **(a, c)** and interpolated to the 100-m

988 depth **(b, d)** from Ctrl averaged over the winters **(a, b)** and summers **(c, d)** of 2015–2018 in Baffin Bay and the

989 Labrador Sea. Winters are defined as December of the previous year to February of that year. Summers are defined

990 as June to August. Current vectors are shown at every 12th grid point. The 1000-m depth contour is shown in gray.
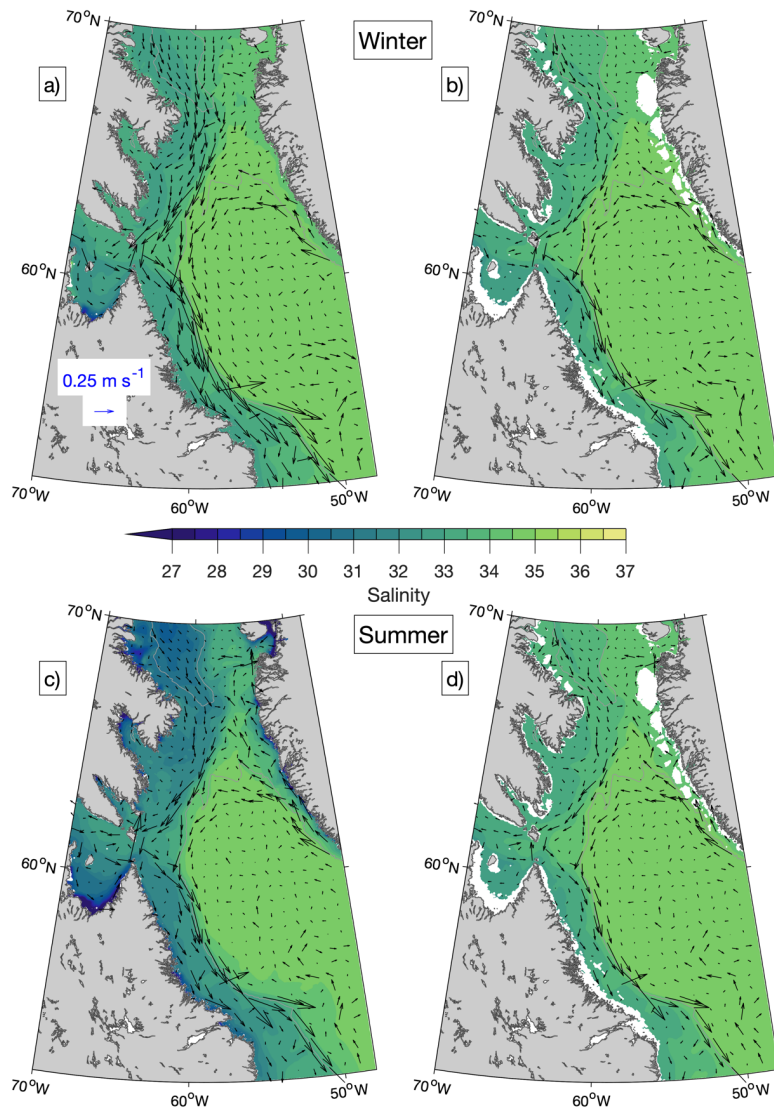
991
992
993   **Figure B2.** Similar to Figure B1 but for Prog.
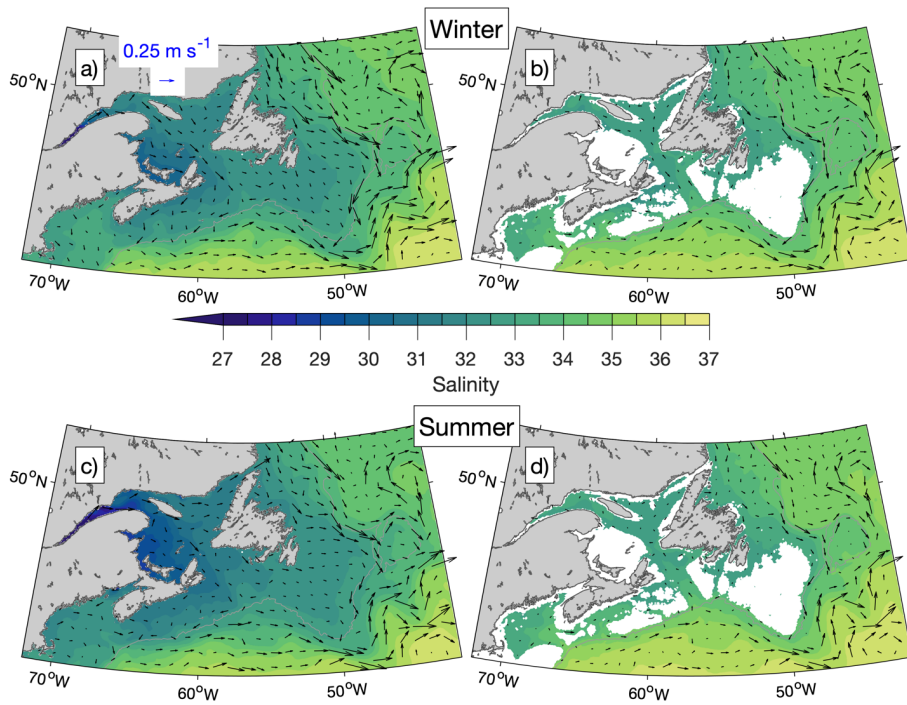
994
995 **Figure B3.** Seasonal-mean simulated salinity and currents at the sea surface **(a, c)** and interpolated to the 100-m
996 depth **(b, d)** from Ctrl averaged over the winters **(a, b)** and summers **(c, d)** of 2015–2018 over the area between the
997 Gulf of Maine and the southern Labrador Sea. Current vectors are shown at every 12th grid point. The 1000-m depth
998 contour is shown in gray.
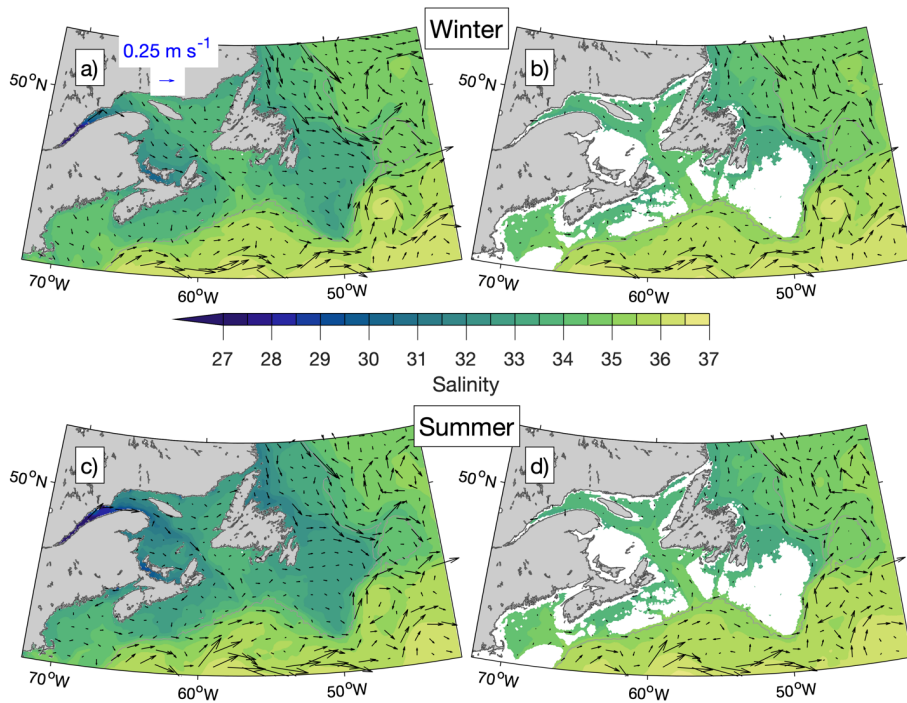
999
1000
Figure B4. Similar to Fig. B3 but for Prog.

Appendix C: Datasets used in model performance assessment

Online sources of the datasets used to assess the model performance are listed below in the order they are discussed in Section 3.

1. Sea surface temperature: OISST v2.1 (Huang et al., 2021), a daily dataset on a 1/4° grid that incorporates satellite and in situ observations. A combination of v2.0 and v2.1 was used in this study; v2.0 is now retired. https://www.ncei.noaa.gov/products/optimum-interpolation-sst

2. Sea surface salinity: MULTIOBS_GLO_PHY_S_SURFACE_MYNRT_015_013 (Buongiorno Nardelli et al., 2016), a dataset that incorporates satellite and in situ observations. At the time of this study, it was a weekly dataset on a 1/4° grid; now it is a daily dataset on a 1/8° grid. https://data.marine.copernicus.eu/product/MULTIOBS_GLO_PHY_S_SURFACE_MYNRT_015_013/description

1013 3. Currents: GLOBAL_MULTIYEAR_PHY_001_030, also known as GLORYS12V1

1014 (Lellouche et al., 2021), a daily reanalysis dataset on a 1/12° grid.

1015 https://data.marine.copernicus.eu/product/GLOBAL_MULTIYEAR_PHY_001_030/descripti

1016 on

1017 4. Shipboard observations of physical and biogeochemical variables: Atlantic Zone Monitoring

1018 Program (Pepin et al., 2005) cruises take place seasonally and Atlantic Zone Off-Shelf

1019 Monitoring Program (e.g., Yashayaev and Loder, 2017) cruises take place annually.

1020 https://catalogue.cioosatlantic.ca/dataset/ca-cioos_9a4bd73f-12a2-40ff-a7c7-b961a1d11311

1021 https://catalogue.cioosatlantic.ca/dataset/ca-cioos_15f90eab-21ed-447d-aea7-8fe98ea27fe5

1022 5. Sea ice: AMSR2 ASI sea ice concentration data for the Arctic, v5.4 (Melsheimer and Spreen,

1023 2019), a daily dataset on a 6.5-km grid derived from satellite observations.

1024 https://doi.pangaea.de/10.1594/PANGAEA.898399

1025 **Code and Data Availability**

1026 The model codes, scripts for compiling the model, and sample CPP header and runtime

1027 parameter files for physics-only simulations are available at

1028 https://doi.org/10.5281/zenodo.12752091 (Ohashi et al., 2024a). Input files used by the ocean

1029 circulation and sea ice modules in a simulation of September – December 2013 are available at

1030 https://doi.org/10.5281/zenodo.12752190 (Ohashi et al., 2024b),

1031 https://doi.org/10.5281/zenodo.12734049 (Ohashi et al., 2024c), and

1032 https://doi.org/10.5281/zenodo.12735153 (Ohashi et al., 2024d). Daily-mean output files from

1033 the ocean circulation, sea ice, and biogeochemistry modules are available for September 2013

1034 (beginning of simulation period) at https://doi.org/10.5281/zenodo.12744506 (Ohashi et al.,

1035 2024e) and for January 2015 (beginning of model validation period) at

1036 https://doi.org/10.5281/zenodo.12746262 (Ohashi et al., 2024f). Input and output files for the

1037 remainder of the simulation period, as well as CPP header, runtime parameter, and input files for

1038 the biogeochemistry module, are available from the corresponding author KO upon request.

Author contributions

KO configured the ocean circulation model; prepared the model bathymetry, freshwater input files, atmospheric forcing files, and some of the lateral boundary input files; and carried out the Prog, NoTides, and NoIce runs. AL prepared input files for and configured the biogeochemical module; and carried out the Ctrl run. CR configured the sea ice model and its coupling to the ocean circulation model; prepared some of the lateral boundary input files and the pseudo-mean versions of freshwater input files; configured the regions used to evaluate model performance; processed the observations used in model evaluation; and calculated the model errors with respect to AZMP observations. AL carried out the analyses for and prepared Figs. 13–15; and wrote the text describing the biogeochemical module, the Ctrl run, and Figs.13–15. KO prepared the rest of the manuscript with advice from JS. JS, KF, and EO provided advice throughout development and evaluation of the model and provided funding to KO, AL, and CR respectively.

Competing interests

The authors declare that they have no conflicts of interest.

Acknowledgements

This study is part of the Ocean Frontier Institute's research project "The Northwest Atlantic Biological Carbon Pump". Simulations were carried out on computing resources maintained by the Digital Research Alliance of Canada. JS, KF, and EO acknowledge support from the National Science and Engineering Research Council of Canada's Discovery Grant program. JS and KO were supported by funding from Fisheries and Oceans Canada (for the project "Modelling ecological connectivity among Canada's Atlantic Marine Protected Areas during the Anthropocene") during preparation of this manuscript. CR was supported by a postdoctoral fellowship from the Marine Environmental Observation, Prediction and Response network (MEOPAR). The authors thank Fehmi Dilmahamod, Xianmin Hu, Bin Wang, and Shengmu Yang for their suggestions and assistance during development of the model. We are also grateful for the constructive comments provided by two anonymous reviewers, which led to the addition of section 3.5 and many other enhancements to the manuscript. Maps in this study were generated

1066   using the package M_Map (Pawlowicz, 2020). The colour maps used in this study are by Thyng

1067   et al. (2016) and Crameri (2018).

1068   **References**

1069   Allen, J. S., Newberger, N. A., and Federiuk, J.: Upwelling circulation on the Oregon continental shelf. Part I:
1070   Response to idealized forcing, J. Phys. Oceanogr., 25(8), 1843–1866, https://doi.org/0.1175/1520-
1071   0485(1995)025%3C1843:UCOTOC%3E2.0.CO;2, 1995.
1072
1073   Babb, D. G., Kirillov, S., Galley, R. J., Straneo, F., Ehn, J. K., Howell, S. E. L., Brady, M., Ridenour, N. A., and
1074   Barber, D. G.: Sea ice dynamics in Hudson Strait and its impact on winter shipping operations, J. Geophys. Res.-
1075   Oceans, 126, e2021JC018024, https://doi.org/10.1029/2021JC018024, 2021.
1076
1077   Bamber, J. L., Tedstone, A. J., King, M. D., Howat, I. M., Enderlin, E. M., van den Broeke, M. R., and Noel, B.:
1078   Land ice freshwater budget of the Arctic and North Atlantic Oceans: 1. Data, methods, and results, J. Geophys.
1079   Res.-Oceans, 123, https://doi.org/10.1002/2017JC013605, 2018.
1080
1081   Bitz, C. M. and Lipscomb, W. H.: An energy-conserving thermodynamic model of sea ice, J. Geophys. Res.,
1082   104(C7), 15669–15677, https://doi.org/10.1029/1999JC900100, 1999.
1083
1084   Bouillon, S., Fichefet, T., Legat, V., and Madec, G.: The elastic-viscous-plastic method revisited, Ocean Model., 71,
1085   2–12, https://doi.org/10.1016/j.ocemod.2013.05.013, 2013.
1086
1087   Bourgault, D. and Koutitonsky, V. G.: Real-time monitoring of the freshwater discharge at the head of the St.
1088   Lawrence Estuary, Atmos.-Ocean, 37(2), 203–220, https://doi.org/10.1080/07055900.1999.9649626, 1999.
1089
1090   Briegleb, B. P. and Light, B.: A Delta-Eddington multiple scattering parameterization for solar radiation in the sea
1091   ice component of the Community Climate System Model, National Center for Atmospheric Research,
1092   https://doi.org/10.5065/D6B27S71, 2007.
1093
1094   Buongiorno Nardelli, B., Droghei, R., and Santoleri, R.: Multi-dimensional interpolation of SMOS sea surface
1095   salinity with surface temperature and in situ salinity, Remote Sens. Environ., 180, 392–402,
1096   https://doi.org/10.1016/j.rse.2015.12.052, 2016.
1097
1098   Cabanes, C., Grouazel, A., von Schuckmann, K., Hamon, M., Turpin, V., Coatanoan, C., Paris, F., Guinehut, S.,
1099   Boone, C., Ferry, N., de Boyer Montégut, C., Carval, T., Reverdin, G., Pouliquen, S., and Le Traon, P.-Y.: The
1100   CORA dataset: validation and diagnostics of in-situ ocean temperature and salinity measurements, Ocean Sci., 9,
1101   1–18, https://doi.org/10.5194/os-9-1-2013, 2013.
1102
1103   Chapman, D. C.: Numerical treatment of cross-shelf open boundaries in a barotropic coastal ocean model, J. Phys.
1104   Oceanogr., 15, 1060–1075, https://doi.org/10.1175/1520-0485(1985)015%3C1060:NTOCSO%3E2.0.CO;2, 1985.
1105
1106   Chassignet, E. P. and Xu, S.: Impact of horizontal resolution (1/12º to 1/50º) on Gulf Stream separation, penetration,
1107   and variability, J. Phys. Oceanogr., 47(8), 1999–2021, https://doi.org/10.1175/JPO-D-17-0031.1, 2017.
1108
1109   Chelton, D., DeSzoeke, R. A., Schlax, M. G, El Naggar, K., and Siwertz, N.: Geographical variability of the first
1110   baroclinic Rossby radius of deformation. J. Phys. Oceanogr., 28(3), 433–460, https://doi.org/10.1175/1520-
1111   0485(1998)028%3C0433:GVOTFB%3E2.0.CO;2, 1998.
1112
1113   Chen, K. and He, R.: Mean circulation in the coastal ocean off northeastern North America from a regional-scale
1114   ocean model. Ocean Sci., 11, 503–517, https://doi.org/10.5194/os-11-503-2015, 2015.
1115
1116   Crameri, F.: Scientific colour maps [software], Zenodo, https://doi.org/10.5281/zenodo.1243862, 2018.

1117
1118   Dai, A.: Dai and Trenberth Global River Flow and Continental Discharge Dataset [data set],
1119   https://doi.org/10.5065/D6V69H1T, 2017.
1120
1121   Drinkwater, K.: On the mean and tidal currents in Hudson Strait, Atmos.-Ocean, 26(2), 252–266,
1122   https://doi.org/10.1080/07055900.1988.9649302, 1988.
1123
1124   Dupont, F., Higginson, S., Bourdalle-Badie, R., Lu, Y., Roy, F., Smith, G. C., Lemieux, J.-F., Garric, G., and
1125   Davidson, F.: A high-resolution ocean and sea-ice modelling system for the Arctic and North Atlantic oceans,
1126   Geosci. Model Dev., 8, 1577–1594, https://doi.org/10.5194/gmd-8-1577-2015, 2015.
1127
1128   Egbert, G. D. and Erofeeva, S. Y.: Efficient inverse modeling of barotropic ocean tides, J. Atmos. Ocean Tech., 19,
1129   183–204, https://doi.org/10.1175/1520-0426(2002)019%3C0183:EIMOBO%3E2.0.CO;2, 2002.
1130
1131   Ezer, T. and Mellor, G. L.: A generalized coordinate ocean model and a comparison of the bottom boundary layer
1132   dynamics in terrain-following and in z-level grids, Ocean Model., 6, 379–403, hppts://doi.org/10.1016/S1463-
1133   5003(03)00026-X, 2004.
1134
1135   Fairall, C. W., Bradley, E. F., Godfrey, J. S., Wick, G. A., Edson, J. B., and Young, G. S.: Cool-skin and warm-layer
1136   effects on sea surface temperature, J. Geophys. Res., 101(C1), 1295–1308, https://doi.org/10.1029/95JC03190,
1137   1996a.
1138
1139   Fairall, C. W., Bradley, E. F., Rogers, D. P., Edson, J. B., and Young, G. S.: Bulk parameterization of air-sea fluxes
1140   for Tropical-Ocean Global Atmosphere Coupled-Ocean Atmosphere Ocean Experiment, J. Geophys. Res.,
1141   101(C2), 3747–3764, https://doi.org/10.1029/95JC03205, 1996b.
1142
1143   Fennel, K., Mattern, J. P., Doney, S., Bopp, L., Moore, A., Wang, B., Yu, L., Ocean biogeochemical modelling, Nat.
1144   Rev. Methods Primers, 2, 76, https://doi.org/10.1038/s43586-022-00154-2, 2022.
1145
1146   Fennel, K., Wilkin, J., Levin, J., Moisan, J., O'Reilly, J., and Haidvogel, D.: Nitrogen cycling in the Middle Atlantic
1147   Bight: Results from a three-dimensional model and implications for the North Atlantic nitrogen budget, Global
1148   Biogeochem. Cy., 20, GB3007, https://doi.org/10.1029/2005GB002456, 2006.
1149
1150   Fennel, K., Wilkin, J., Previdi, M., and Najjar, R.: Denitrification effects on air-sea CO_2 flux in the coastal ocean:
1151   Simulations for the northwest North Atlantic, Geophys. Res. Lett., 35, L24608,
1152   https://doi.org/10.1029/2008GL36147, 2008.
1153
1154   Fennel, K., Hu, J., Laurent, A., Marta-Almeida, M., and Hetland, R.: Sensitivity of hypoxia predictions for the
1155   north- ern Gulf of Mexico to sediment oxygen consumption and model nesting, J. Geophys. Res.-Oceans, 118,
1156   990–1002, https://doi.org/10.1002/jgrc.20077, 2013.
1157
1158   Frajka-Williams, E. and Rhines, P. B.: Physical controls and interannual variability of the Labrador Sea spring
1159   phytoplankton bloom in distinct regions, Deep-Sea Res. Pt. I, 57, 541–552,
1160   https://doi.org/10.1016/j.dsr.2010.01.003, 2010.Garçon, V. C., Oschlies, A., Doney, S. C., McGillicuddy, D.,
1161   Waniek, J.: The role of mesoscale variability on plankton dynamics in the North Atlantic, Deep-Sea Res. Pt. II, 48,
1162   2199–2226, https://doi.org/10.1016/S0967-0645(00)00183-1, 2001.
1163
1164   Gatien, M. G.: A study in the slope water region south of Halifax, J. Fish. Res. Board Can., 33(10), 2213–2217,
1165   https://doi.org/10.1139/f76-270, 1976.
1166
1167   GEBCO Compilation Group: GEBCO 2019 Grid [data set], https://doi.org/10.5285/836f016a-33be-6ddc-e053-
1168   6c86abc0788e, 2019.
1169
1170   Haidvogel, D. B., Arango, H., Budgell, W. P., Cornuelle, B. D., Curchister, E., Di Lorenzo, E., Fennel, K., Geyer, W.
1171   R., Hermann, A. J., Lanerolle, L., Levin, J., McWilliams, J. C., Miller, A. J., Moore, A. M., Powell, T. M.,
1172   Shchepetkin, A. F., Sherwood, C. R., Signell, R. P., Warner, and Wilkin, J.: Ocean forecasting in terrain-following

1173   coordinates: Formulation and skill assessment of the Regional Ocean Modeling System, J. Comput. Phys., 227,
1174   3595–3624, https://doi.org/10.1016/j.jcp.2007.06.016, 2008.
1175
1176 Han, G., Hannah, C. G., Loder, J. W., and Smith, P. C.: Seasonal variation of the three-dimensional mean circulation
1177   over the Scotian Shelf, J. Geophys. Res., 102(C1), 1011–1025, https://doi.org/10.1029/96JC03285, 1997.
1178
1179 Hedstrom, K. S.: Technical manual for a coupled sea-ice/ocean circulation model (Version 5), U.S. Dept. of the
1180   Interior, Bureau of Ocean Energy Management, Alaska OCS Region, 2018.
1181
1182 Hersbach, H., Bell, B., Berrisford, P., Biavati, G., Horányi, A., Muñoz Sabater, J., Nicolas, J., Peubey, C., Radu, R.,
1183   Rozum, I., Schepers, D., Simmons, A., Soci, C., Dee, D., Thépaut, J.-N.: ERA5 hourly data on single levels from
1184   1979 to present [data set], Copernicus Climate Change Service Climate Data Store,
1185   https://doi.org/10.24381/cds.adbb2d47, 2018.
1186
1187 Huang, B., Liu, C., Banzon, V., Freeman, E., Graham, G., Hankins, B., Smith, T., and Zhang, H.-M..: Improvements
1188   of the Daily Optimum Interpolation Sea Surface Temperature (DOISST) Version 2.1, J. Climate, 34, 2923–2939,
1189   https://doi.org/10.1175/JCLI-D-20-0166.1, 2021.
1190
1191 Hunke, E. C. and Dukowicz, J. K.: An elastic-viscous-plastic model for sea ice dynamics, J. Phys. Oceanogr., 27,
1192   1849–1867, https://doi.org/10.1175/1520-0485(1997)027%3C1849:AEVPMF%3E2.0.CO;2, 1997.
1193
1194 Hunke, E. C., Lipscomb, W. H., Turner, A. K., Jeffery, N., and Elliott, S.: CICE: The Los Alamos sea ice model
1195   documentation and software user's manual version 5.1 LA-CC-06-012, Los Alamos National Laboratory, 2015.
1196
1197 Ikeda, M., Yao, T., and Yao, Q.: Seasonal evolution of sea ice cover and shelf water off Labrador simulated in a
1198   coupled ice-ocean model, J. Geophys. Res., 101(C7), 16465–16489, https://doi.org/10.1029/96JC00716, 1996.
1199
1200 Jacob, R., Larson, J., and Ong, E.: M x N communication and parallel interpolation in Community Climate System
1201   Model version 3 using the Model Coupling Toolkit, Int. J. High Perform. Comput. Appl., 19(3), 293–307,
1202   https://doi.org/10.1177/1094342005056116, 2005.
1203
1204 Jin, M., Deal, C., Maslowski, W., Matrai, P., Roberts, A., Osinski, R., Lee, Y. J., Frants, M., Elliott, S., Jefferey, N.,
1205   Hunke, E., and Wang, S.: Effects of model resolution and ocean mixing on forced ice-ocean physical and
1206   biogeochemical simulations using global and regional system models, J. Geophys. Res.-Oceans, 123, 358–377,
1207   https://doi.org/10.1002/2017JC013365, 2018.
1208
1209 Johnson, K. S. and Claustre, H.: Bringing biogeochemistry into the Argo age, Eos, 97,
1210   https://doi.org/10.1029/2016EO062427, 2016.
1211
1212 Killworth, P. D.: Time interpolation of forcing fields in ocean models, J. Phys. Oceanogr., 26(1), 136-143,
1213   https://doi.org/10.1175/1520-0485(1996)026%3C0136:TIOFFI%3E2.0.CO;2.
1214
1215 Körtzinger, A., Send, U., Wallace, D. W. R., Karstensen, J., and DeGrandpre, M.: Seasonal cycle of O_2 and PCO_2 in
1216   the central Labrador Sea: Atmospheric, biological, and physical implications, Global Biogeochem. Cy., 22,
1217   GB1014, https://doi.org/10.1029/2007GB003029, 2008.
1218
1219 Kristensen, N. M., Debernard, J. B., Maartenson, S., Wang, K., and Hedstrom, K.: metno/metroms: Version 0.3 -
1220   before merge (v0.3) [code], Zenodo, https://doi.org/10.5281/zenodo.1046114, 2017.
1221
1222 Larson, J., Jacob, R., Ong, E.: The Model Coupling Toolkit: A new Fortran90 toolkit for building Multiphysics
1223   parallel coupled models, Int. J. High Perform. Comput. Appl., 19(3), 277–292,
1224   https://doi.org/10.1177/1094342005056115, 2005.
1225
1226 Laurent, A., Fennel, K., and Kuhn, A.: An observation-based evaluation and ranking of historical Earth system
1227   model simulations in the northwest North Atlantic Ocean, Biogeosciences, 18, 1803–1822,
1228   https://doi.org/10.5194/bg-18-1803-2021, 2021.

Lauvset, S. K., Lange, N., Tanhua, T., Bittig, H. C., Olsen, A., Kozyr, A., Álvarez, M., Becker, S., Brown, P. J., Carter, B. R., Cotrim da Cunha, L., Feely, R. A., van Heuven, S., Hoppema, M., Ishii, M., Jeansson, E., Jutterström, S., Jones, S. D., Karlsen, M. K., Lo Monaco, C., Michaelis, P., Murata, A., Pérez, F. F., Pfeil, B., Schirnick, C., Steinfeldt, R., Suzuki, T., Tilbrook, B., Velo, A., Wanninkhov, R., Woosley, R. J., and Key, R. M.: An updated version of the global interior ocean biogeochemical data product, GLODAPv2.2021, Earth Syst. Sci. Data, 13, 5565–5589, https://doi.org/10.5194/essd-13-5565-2021, 2021.

Lavender, K. L., Davis, R. E., and Brechner, O. W.: Mid-depth recirculation observed in the interior Labrador and Irminger seas by direct velocity measurements, Nature, 407, 66–69, https://doi.org/10.1038/35024048, 2000.

Lavoie, D., Lambert, N., Starr, M., Chassé, J., Riche, O., Le Clainche, Y., Azetsu-Scott, K., Béjaoui, B., Christian, J. R., and Gilbert, D.: The Gulf of St. Lawrence Biogeochemical Model: A management tool for fisheries and ocean management, Front. Mar. Sci., 8, 732269, https://doi.org/10.3389/fmars.2021.732269, 2021.

Le Fouest, V., Zakardjian, B., and Saucier, F. J.: Plankton ecosystem response to freshwater-associated bulk turbidity in the subarctic Gulf of St. Lawrence (Canada): A modelling study, J. Marine Syst., 81, 75–85, https://doi.org/10.1016/j.jmarsys.2009.12.003, 2010.

Legendre, L., Ackley, S. F., Dieckmann, G. S., Gulliksen, B., Horner, R., Hoshiai, T., Melnikov, I. A., Reeburgh, W. S., Spindler, M., and Sullivan, C. W: Ecology of sea ice biota: 2. Global significance, Polar Biol., 12, 429–444, https://doi.org/10.1007/bf00243114, 1992.

Lellouche, J.-M., Greiner, E., Le Galloudec, O., Garric, G., Regnier, C., Drevillon, M., Benkiran, M., Testut, C.-E., Bourdalle-Badie, R., Gasparin, F., Hernandez, O., Levier, B., Drillet, Y., Remy, E., and Le Traon, P.-Y. : Recent updates to the Copernicus Marine Service global ocean monitoring and forecasting real-time 1/12° high-resolution system, Ocean Sci., 14, 1093–1126, https://doi.org/10.5194/os-14-1093-2018, 2018.

Lellouche, J.-M., Greiner, E., Bourdallé-Badie, R., Garric, G., Melet, A., Drévillon, M., Clement, B., Hamon, M., Le Galloudec, O., Regnier, C., Candela, T., Testut, C.-E., Gasparin, F., Ruggiero, G., Mounir, B., Yann, D., and Le Traon, P.-Y. : The Copernicus Global 1/12º Oceanic and Sea Ice GLORYS12 Reanalysis, Front. Earth Sci., 9, 698876, https://doi.org/10.3389/feart.2021.698876, 2021.

Lipscomb, W. H. and Hunke, E. C.: Modeling sea ice transport using incremental mapping, Mon. Weather Rev., 132(6), 1341–1354, https://doi.org/10.1175/1520-0493(2004)132%3C1341:MSITUI%3E2.0.CO;2, 2004.

Lu, Y., Higginson, S., Nudds, S., Prinsenberg, S., and Garric, G.: Model simulated volume fluxes through the Canadian Arctic Archipelago and Davis Strait: Linking monthly variations to forcings in different seasons, J. Geophys. Res.-Oceans, 119, 1927–1942, https://doi.org/10.1002/2013JC009408, 2014.

Luo, H., Bracco, A., and Zhang, F.: The seasonality of convective events in the Labrador Sea, J. Clim., 27(17), 6456–6471, https://doi.org/10.1175/JCLI-D-14-00009.1, 2014.

Ma, Z., Han, G., and Chassé, J.: Simulation of circulation and ice over the Newfoundland and Labrador Shelves: The mean and seasonal cycle, Atmos.-Ocean, 54(3), 248–263, https://doi.org/10.1080/07055900.2015.1077325, 2016.

Marchesiello, P., McWilliams, J. C., and Shchepetkin, A.: Open boundary conditions for long-term integration of regional oceanic models, Ocean Model., 3, 1–20, https://doi.org/10.1016/S1463-5003(00)00013-5, 2001.

Marchesiello, P., Debreu, L., Couvelard, X.: Spurious diapycnal mixing in terrain-following coordinate models: The problem and a solution, Ocean Model., 26, 156–169, https://doi.org/10.1016/j.ocemod.2008.09.004, 2009.

Martz, T. R., DeGrandpre, M. D., Strutton, P. G., McGillis, W. R., and Drennan, W. M.: Sea surface pCO_2 and carbon export during the Labrador Sea spring-summer bloom: An in situ mass balance approach, J. Geophys. Res., 114, C09008, https://doi.org/10.1029/2008JC005060, 2009.

1285
1286 Mason, E., Molemaker, J., Shchepetkin, A. F., Colas, F., McWilliams, J. C., and Sangrà, P.: Procedures for offline
1287 grid nesting in regional ocean models, Ocean Model., 35, 1–15, https://doi.org/10.1016/j.ocemod.2010.05.007,
1288 2010.
1289
1290 McDougall, T. M. and Barker, P. M.: Getting started with TEOS-10 and the Gibbs Seawater (GSW) Oceanographic
1291 Toolbox, SCOR/IAPSO WG127, ISBN 978-0-646-55621-5, 2011.
1292
1293 Melsheimer, C. and Spreen, G.: AMSR2 ASI sea ice concentration data, Arctic, version 5.4 (NetCDF) (June 2012 -
1294 December 2018) [data set], PANGAEA, https://doi.org/10.1594/PANGAEA.898399, 2019.
1295
1296 Mellor, G. L. and Yamada, T.: Development of a turbulence closure model for geophysical fluid problems, Rev.
1297 Geophys. and Space Phys., 20(4), 851–875, https://doi.org/10.1029/RG020i004p00851, 1982.
1298
1299 Mysak, L. A., Peng, S., and Wood, R. G.: Application of a coupled ice-ocean model to the Labrador Sea, Atmos.-
1300 Ocean, 29(2), 232–255, https://doi.org/10.1080/07055900.1991.9649404, 1991.
1301
1302 Naughten, K. A., Galton-Fenzi, B. K., Meissner, K. J., England, M. H., Brassington, G. B., Colberg, F., Hatterman,
1303 T., and Debernard, J. B.: Spurious sea ice formation caused by oscillatory ocean tracer advection schemes, Ocean
1304 Model., 116, 108–117, https://doi.org/10.1016/j.ocemod.2017.06.010, 2017.
1305
1306 Ohashi, K., Laurent, A., Renkl, C.: Sheng: J., Fennel, K., and Oliver, E.:DALROMS-NWA12 v1.0, a coupled
1307 circulation-sea ice-biogeochemistry model for the northwest North Atlantic: codes and namelists (Version v3)
1308 [software], Zenodo, https://doi.org/10.5281/zenodo.12752091, 2024a.
1309
1310 Ohashi, K., Laurent, A., Renkl, C., Sheng, J., Fennel, K., and Oliver, E.: DALROMS-NWA12 v1.0, a coupled
1311 circulation-sea ice-biogeochemistry model for the northwest North Atlantic: input files (1 of 3) (Version v2) [data
1312 set], Zenodo, https://doi.org/10.5281/zenodo.12752190, 2024b.
1313
1314 Ohashi, K., Laurent, A., Renkl, C., Sheng, J., Fennel, K., and Oliver, E.: DALROMS-NWA12 v1.0, a coupled
1315 circulation-sea ice-biogeochemistry model for the northwest North Atlantic: input files (2 of 3) (Version v1) [data
1316 set], Zenodo, https://doi.org/10.5281/zenodo.12734049, 2024c.
1317
1318 Ohashi, K., Laurent, A., Renkl, C., Sheng, J., Fennel, K., and Oliver, E.: DALROMS-NWA12 v1.0, a coupled
1319 circulation-sea ice-biogeochemistry model for the northwest North Atlantic: input files (3 of 3) (Version v1) [data
1320 set], Zenodo, https://doi.org/10.5281/zenodo.12735153, 2024d.
1321
1322 Ohashi, K., Laurent, A., Renkl, C., Sheng, J., Fennel, K., and Oliver, E.: DALROMS-NWA12 v1.0, a coupled
1323 circulation-sea ice-biogeochemistry model for the northwest North Atlantic: output files (1 of 2) (Version v1) [data
1324 set], Zenodo, https://doi.org/10.5281/zenodo.12744506, 2024e.
1325
1326 Ohashi, K., Laurent, A., Renkl, C., Sheng, J., Fennel, K., and Oliver, E.: DALROMS-NWA12 v1.0, a coupled
1327 circulation-sea ice-biogeochemistry model for the northwest North Atlantic: output files (2 of 2) (Version v1) [data
1328 set], Zenodo, https://doi.org/10.5281/zenodo.12746262, 2024f.
1329
1330 Pawlowicz, R.: M_Map: A mapping package for MATLAB, version 1.4m [software],
1331 https://www.eoas.ubc.ca/~rich/map.html, 2020.
1332
1333 Pei, Q.: Study of circulation, hydrography and dissolved oxygen concentration over coastal waters of the Scotian
1334 Shelf, M.Sc. thesis, Dalhousie University, http://hdl.handle.net/10222/81682, 2022.
1335
1336 Pennelly, C. and Myers, P. G.: Introducing LAB60: A 1/60º NEMO 3.6 numerical simulation of the Labrador Sea,
1337 Geosci. Model Dev., 13, 4959–4975, https://doi.org/10.5194/gmd-13-4959-2020, 2020.
1338
1339 Pepin, P., Petrie, B., Therriault, J.-C., Narayanan, S., Harrison, W. G., Frank, K. T., Chassé, J., Colbourne, E. B.,
1340 Gilbert, D., Gregory, D., Harvey, M., Maillet, G. L., Mitchell, M., and Starr, M.: The Atlantic Zone Monitoring

Program (AZMP): Review of 1998–2003 (Can. Tech. Rep. Hydrogr. Ocean Sci. 242), Fisheries and Oceans Canada, 2005.

Prinsenberg, S. J. and Peterson, I. K.: Sea-ice properties off Labrador and Newfoundland during LIMEX '89, Atmos.-Ocean, 30(2), 207–222, https://doi.org/10.1080/07055900.1992.9649438, 1992.

Rhein, M., Steinfeldt, R., Kieke, D., Stendardo, I., and Yashayaev, I.: Ventilation variability of Labrador Sea Water and its impact on oxygen and anthropogenic carbon: a review, Phil. Trans. R. Soc. A, 375, 20160321, https://doi.org/10.1098/rsta.2016.0321, 2017.

Richaud, B., Fennel, K., Oliver, E. C. J., DeGrandpre, M. D., Bourgeois, T., Hu, X., and Lu, Y.: Underestimation of oceanic carbon uptake in the Arctic Ocean: ice melt as predictor of the sea ice carbon pump, Cryosphere, 17, 2665–2680, https://doi.org/10.5194/tc-17-2665-2023, 2023.

Richaud, B., Kwon, Y.-O., Joyce, T. M., Fratantoni, P. S., and Lentz, S. J.: Surface and bottom temperature and salinity climatology along the continental shelf off the Canadian and U.S. east coasts, Cont. Shelf Res., 124, 165–181, https://doi.org/10.1016/j.csr.2016.06.005, 2016.

Ridenour, N. A., Hu, X., Sydor, K., Myers, P. G., and Barber, D. G.: Revisiting the circulation of Hudson Bay: Evidence for a seasonal pattern, Geophys. Res. Lett., 46, 3891–3899, https://doi.org/10.1029/2019GL082344, 2019.

Ross, A. C., Stock, C. A., Adcroft, A., Curchitser, E., Hallberg, R., Harrison, M. J., Hedstrom, K., Zadeh, N., Alexander, M., Chen, W., Drenkard, E. J., du Pontavice, H., Dussin, R., Gomez, F., John, J. G., Kang, D., Lavoie, D., Resplandy, L., Roobaert, A., Saba, V., Shin, S., Siedlecki, S., and Simkins, J.: A high-resolution physical-biological model for marine resource applications in the northwest Atlantic (MOM6-COBALT-NWA12 v1.0), Geosci. Model Dev., 16, 6943–6985, https://doi.org/10.5194/gmd-16-6943-2023, 2023.

Rutherford, K. and Fennel, K.: Elucidating coastal ocean carbon transport processes: A novel approach applied to the northwest North Atlantic shelf, Geophys. Res. Lett., 49, e2021GL097614, https://doi.org/10.1029/2021GL097614, 2022.

Saucier, F. J., Senneville, S., Prinsenberg, S., Roy, F., Smith, G., Gachon, P., Caya, D., and Laprise, R.: Modelling the sea ice-ocean seasonal cycle in Hudson Bay, Foxe Basin and Hudson Strait, Canada, Clim. Dynam., 23, 303–326, https://doi.org/10.1007/s00382-004-0445-6, 2004.

Schwab, D. J., Clites, A. H., Murthy, C. R., Sandall, J. E., Meadows, L. R., and Meadows, G. A.: The effect of wind on transport and circulation in Lake St. Clair, J. Geophys. Res., 94(C4), 4947–4958, https://doi.org/10.1029/JC094iC04p04947, 1989.

Shapiro, R.: Linear filtering, Math. Comput., 19(132), 1094–1097, https://doi.org/10.1090/S0025-5718-1975-0389356-X, 1975.

Sheng, J.: Circulation and drift pathways in the northwest Atlantic Ocean, in: Estuarine and Coastal Modeling: Proceedings of the Seventh International Conference, St. Petersburg, FL, 5–7 November 2001, 364–383, https://doi.org/10.1061/40628(268)23, 2002.

Smith, G. C., Roy, F., and Brasnett, B.: Evaluation of an operational ice-ocean analysis and forecasting system for the Gulf of St. Lawrence, Q. J. Roy. Meteor. Soc., 139, 419–433, https://doi.org/10.1002/qj.1982, 2013.

Song, Y. and Haidvogel, D.: A semi-implicit ocean circulation model using a generalized topography-following coordinate system. J. Comput. Phys., 115(1), 228-244, https://doi.org/10.1006/jcph.1994.1189.

St. Lawrence Global Observatory: Freshwater runoffs of the St. Lawrence at the height of Québec City [data set], https://catalogue.ogsl.ca/dataset/ca-cioos_84a17ffc-4898-4261-94de-4a5ea2a9258d?local=en, 2023.

1397 Strutton, P. G., Martz, T. R., DeGrandpre, M. D., McGillis, W. R., Drennan, W. M., and Boss, E.: Bio-optical
1398 observations of the 2004 Labrador Sea phytoplankton bloom, J. Geophys. Res., 116, C11037,
1399 https://doi.org/10.1029/2010JC006872, 2011.
1400
1401 Szekely, T.: Product user manual: In situ TAC objective analysis products, v1.11, Mercator Ocean International,
1402 2023.
1403
1404 Takahashi, T., Sutherland, S. C., Wanninkhof, R., Sweeney, C., Feely, R.A., Chipman, D. W., Hales, B., Friederich,
1405 G., Chavez, F., Sabine, C., Watson, A., Bakker, D. C. E., Schuster, U., Metzl, N., Yoshikawa-Inoue, H., Ishii, M.,
1406 Midorikawa, T., Nojiri, Y., Körtzinger, A., Steinhoff, T., Hoppema, M., Olafsson, J., Arnarson, T. S., Tilbrook, B.,
1407 Johannessen, T., Olsen, A., Bellerby, R., Wong, C. S., Delille, B., Bates, N. R., de Barr, H. J. W., Climatological
1408 mean and decadal change in surface ocean pCO_2, and net sea-air CO_2 flux over the global oceans, Deep-Sea Res.
1409 Pt. II, 56, 554–577, https://doi.org/10.1016/j.dsr2.2008.12.009, 2009.
1410
1411 Tang, C. L., Gui, Q., and DeTracey, B. M.: A modeling study of upper ocean winter processes in the Labrador Sea, J.
1412 Geophys. Res., 104(C10), 23411–23425, https://doi.org/10.1029/1999JC900214, 1999.
1413
1414 The Lab Sea Group: The Labrador Sea Deep Convection Experiment, B. Am. Meteorol. Soc., 79(10), 2033–2058,
1415 https://doi.org/10.1175/1520-0477(1998)079%3C2033:TLSDCE%3E2.0.CO;2, 1998.
1416
1417 Thyng, K. M., Greene, C. A., Hetland, R. D., Zimmerle, H. M., and DiMarco, S. F.: True colors of oceanography:
1418 Guidelines for effective and accurate colormap selection. Oceanography, 29(3), 9-13,
1419 https://doi.org/10.5670/oceanog.2016.66, 2016.
1420
1421 Tian, R. C., Deibel, D., Rivkin, R. B., and Vézina, A. F.: Biogenic carbon and nitrogen export in a deep-convection
1422 region: simulations in the Labrador Sea, Deep-Sea Res. Pt. I, 51, 413–437,
1423 https://doi.org/10.1016/j.dsr.2003.10.015, 2004.
1424
1425 Urrego-Blanco, U., and Sheng, J.: Study on subtidal circulation and variability in the Gulf of St. Lawrence, Scotian
1426 Shelf, and Gulf of Maine using a nested-grid shelf circulation model, Ocean Dynam., 64, 385–412,
1427 https://doi.org/10.1007/s10236-013-0688-z, 2014.
1428
1429 Volk, T. and Hoffert, M. I.: Ocean carbon pumps: Analysis of relative strengths and efficiencies in ocean-driven
1430 atmospheric CO2 changes, in: The carbon cycle and atmospheric CO2: Natural variations Archean to present,
1431 Geoph. Monog. Series vol. 32, edited by Sundquist, E. T. and Broecker, W. S., 99–110,
1432 https://doi.org/10.1029/GM032p0099, 1985.
1433
1434 Wang, B., Fennel, K., An assessment of vertical carbon flux parameterizations using backscatter data from BGC
1435 Argo, Geophys. Res. Lett., https://doi.org/10.1029/2022GL101220, 2023.
1436
1437 Wang, B., Fennel, K., Biogeochemical Argo data suggest only a minor contribution of small particles to long-term
1438 carbon sequestration in the subpolar North Atlantic, Limnol. Oceanogr., https://doi.org/10.1002/lno.12209, 2022.
1439
1440 Wang, Y., Sheng, J., and Lu, Y.: Examining tidal impacts on seasonal circulation and hydrography variability over
1441 the eastern Canadian shelf using a coupled circulation-ice regional model, Prog. Oceanogr., 189, 102448,
1442 https://doi.org/10.1016/j.pocean.2020.102448, 2020.
1443
1444 Wang, Z., Lu, Y., Greenan, B., Brickman, D., and DeTracey, B.: BNAM: An eddy-resolving North Atlantic Ocean
1445 model to support ocean monitoring. (Can. Tech. Rep. Hydrogr. Ocean Sci. 327), Fisheries and Oceans Canada,
1446 2018.
1447
1448 Wu, Y., Peterson, I. K., Tang, C. C. L., Platt, T., Sathyendranath, S., and Fuentes-Yaco, C.: The impact of sea ice on
1449 the initiation of the spring bloom on the Newfoundland and Labrador Shelves, J. Plankton Res., 29(6), 509–514,
1450 https://doi.org/10.1093/plankt/fbm035, 2007.
1451

1452 Wu, Y., Platt, T., Tang, C. C. L., and Sathyendranath, S.: Regional differences in the timing of the spring bloom in
1453   the Labrador Sea, Mar. Ecol. Prog. Ser., 355, 9–20, https://doi.org/10.3354/meps07233, 2008.
1454

1455 Wu, Y., Tang, C., and Hannah, C.: The circulation of eastern Canadian seas, Prog. Oceanogr., 106, 28–48,
1456   https://doi.org/10.1016/j.pocean.2012.06.005, 2012.
1457

1458 Wu, H. and Zhu, J.: Advection scheme with 3rd high-order spatial interpolation at the middle temporal level and its
1459   application to saltwater intrusion in the Changjiang Estuary, Ocean Model., 33(1–2), 33–51,
1460   https://doi.org/10.1016/j.ocemod.2009.12.001, 2010.
1461

1462 Yang, B., Fox, J., Behrenfeld, M. J., Boss, E. S., Haëntjens, N., Halsey, K. H., Emerson, S. R., and Doney, S. C..: In
1463   situ estimates of net primary production in the western North Atlantic with Argo profiling floats, J. Geophys.
1464   Res.-Biogeo., 126, e2020JG06116, https://doi.org/10.1029/2020JG006116, 2020.
1465

1466 Yang, S., Sheng, J., Ohashi, K., Yang, B., Chen, S., Xing, J.: Non-linear interactions between tides and storm surges
1467   during extreme weather events over the eastern Canadian shelf, Ocean Dynam., 73, 279–301,
1468   https://doi.org/10.1007/s10236-023-01556-w, 2023.
1469

1470 Yao, T., Tang, C. L., and Peterson, I. K.: Modeling the seasonal variation of sea ice in the Labrador Sea with a
1471   coupled multicategory ice model and the Princeton Ocean Model, J. Geophys. Res., 105(C1), 1153–1165,
1472   https://doi.org/10.1029/1999JC900264, 2000.
1473

1474 Yashayaev, I.: Intensification and shutdown of deep convection in the Labrador Sea were caused by changes in
1475   atmospheric and freshwater dynamics, Commun. Earth Environ., 5, 1–23, https://doi.org/10.1038/s43247-024-
1476   01296-9, 2024.
1477

1478 Yashayaev, I. and Loder, J. W.: Further intensification of deep convection in the Labrador Sea in 2016, Geophys.
1479   Res. Lett., 44(3), 1429–1438, https://doi.org/10.1002/2016GL071668, 2017.
1480

1481 Zhang, S., Sheng, J., and Greatbatch, R. J.: A coupled ice-ocean modeling study of the northwest Atlantic Ocean, J.
1482   Geophys. Res., 109, C04009, https://doi.org/10.1029/2003JC001924, 2004.
1483